AN ABSTRACT OF THE THESIS OF

Rigel Flora for the degree of Master of Science in Radiation Health Physics presented on November 19, 2020.

Title: Dosimetric Evaluation of Nasal Cavity Basal Cell Layer During Radiotracer Administration

Abstract approved:

_____

David M. Hamby

New delivery methods for radiotracers are constantly being proposed. Two key properties of the delivery method must be analyzed: dose to patient and effectiveness of delivery. In this work, the localized skin dose for intranasal administration of ^{18}F was determined utilizing MCNP code. An anatomically accurate nasal cavity was constructed and then several different distributions were simulated. These results were then compared to VARSKIN, a computational software designed specifically for skin dose. Both codes indicate the same result, for the typical administration of 185 MBq, the local skin dose exceeds any reasonable level and poses a very high risk to the patient. Because of this, intranasal administration of ^{18}F cannot be recommended for medical use.

Dosimetric Evaluation of Nasal Cavity Basal Cell Layer during Radiotracer Administration

by
Rigel Flora

A THESIS

submitted to

Oregon State University

in partial fulfillment of
the requirements for the
degree of

Master of Science

Presented November 19, 2020
Commencement June 2021

Master of Science thesis of Rigel Flora presented on November 19, 2020.

APPROVED:

Major Professor, representing Radiation Health Physics

Head of the School of Nuclear Science and Engineering

Dean of the Graduate School

I understand that my thesis will become part of the permanent collection of Oregon State University libraries. My signature below authorizes release of my thesis to any reader upon request.

Rigel Flora, Author

ACKNOWLEDGEMENTS

I would like to give special thanks to Dr. David M. Hamby. Not only for being an excellent instructor and mentor during my time at OSU, but also going above and beyond to ensure the success of his students. It is rare to find an individual as dedicated to helping others as he is. I will never forget when he quite literally ran me down in the hallway to ensure I did not need extra help after a poor quiz grade. Truly an excellent example of a committed professor.

TABLE OF CONTENTS

LIST OF FIGURES

LIST OF TABLES

LIST OF APPENDICES

Dosimetric Evaluation of Nasal Cavity Basal Cell Layer during Radiotracer Administration

1) Introduction

Advances in medicine are omnipresent and seem to only be accelerating. Currently, there is a large interest in alternate delivery routes for pharmaceuticals, including radiotracers. The region which restricts access the most and presents the greatest difficulty to treat is undoubtedly the central nervous system (Wang, 2019). It is shielded by a largely impermeable membrane called the blood brain barrier (BBB). It prevents nearly 100% of all pharmaceuticals and radioligands from passing (Gao, 2013).

Pharmaceutical research may provide a solution. Currently, intranasal administration of pharmaceuticals is being used to deliver medicine directly to the brain to treat diseases such as Alzheimer's (Freiherr, 2013). Normally, the BBB would not allow compounds such as insulin or oxytocin to interact with the brain (Gao, 2013). When applied intranasally, however, the pharmaceuticals can bypass the BBB entirely and be transported directly into the CNS tissue (Wang, 2019).

This is not only exciting for pharmaceutical treatments, but the use of this pathway could also be extended to imaging purposes. By allowing radiotracers direct access to the brain, it opens up a host of new radiotracers which could potentially be used. Currently, the most popular radioligand for brain imaging is fluorodeoxyglucose, [^{18}F]FDG for short (Miele, 2008). It consists of two parts, a F-18 nuclide attached to a glucose molecule. The glucose acts as the transport, and the F-18 nuclide as the radiological tag (Chaly, 2010). [^{18}F]FDG is the leading choice for brain imaging

because glucose is able to cross the BBB, bringing with it the positron source (Miele, 2008).

The downside, however, is that the rest of the body also requires glucose. Meaning the radioligand is transported to all regions of the body - it cannot be exclusively targeted to the brain (Miele, 2008). Because of this, a substantial radiation dose is required to ensure sufficient activity within the brain for imaging (Chaly, 2010). By bypassing the BBB and transporting the radioligands to the brain, it may be possible to lower whole body dose to the patient.

As with all shifts in procedure, there is a tradeoff. When introduced intravenously, the radioligand is quickly distributed away from the area of application limiting local dose (Miele, 2008). In intranasal administration, however, the radioligand will remain concentrated within the sinus cavity for a longer period of time (Singh, 2018). Due to the increased concentration and duration, far more decays will occur within the nasal cavity and thus impart a much higher dose. The primary dosimetric concern is the localized tissue dose. ICRP has strict regulations regarding dose limits, though for medical procedures the area does grey slightly (ICRP 2000). There is, however, an ethical limit which will prevent the use of this administration route if the dosage is high enough to cause harm to the patient.

Utilizing Monte Carlo simulation, this thesis intends to tackle the issue of local tissue dose in the nasal cavity. A replication of the nasal cavity was created for the simulation and ^{18}F was “deposited” on the tissue surface. This model was then analyzed and an approximation of dose across the basal layer was generated. From this, a conclusion was drawn whether the intranasal administration route is viable.

2) Literature Review

2.1) BBB

A selective barrier between the blood stream and brain was inadvertently discovered in the late 19th century by German physicist Paul Ehrlich when he injected a dye directly into a mouse's bloodstream. Upon dissection, he discovered that the dye permeated all tissues within the mouse except for brain and spinal cord (Ehrlich, 1885) At that time, however, an incorrect conclusion was drawn. Ehrlich stated that this was likely due to a low affinity for the dye from the central nervous tissue (Ehrlich, 1885). It was another 15 years until a student of his correctly hypothesized there existed a capillary boundary between the blood stream and central nervous system (CNS) (Lewandowski, 1900). He noticed that when pharmacological agents were administered intravenously, they had no effect upon the CNS. When applied directly to the CNS, however, the expected neurological effects took place. With this information, Lewandowski correctly deduced the existence of a selective membrane and coined it the blood brain barrier (BBB).

This concept, however, was a highly debated matter. Many arguments took place whether or not such a barrier could exist. These came to a climax with the invention of the electron microscope. In 1957, Maynard, Shultz, and Pease (1957), claimed the postulation of such a barrier unnecessary due to new images which showed a lack of extracellular fluid. The theory being – slow uptake of extracellular substances in CNS tissue could be accounted for by the lack of fluid. While this theory is already questionable due to certain substances being unable to penetrate CNS tissue at all, it was still tested. An *in vitro* study was organized where brain

tissue was tested alongside muscle tissue to determine penetration rates of common extracellular substances. It was found that penetration rates between the two were nearly identical – thus confirming the existence of the BBB (Davson and Spaziani, 1959). This immediately spurred further research into compounds capable of bypassing the BBB.

2.2) Permeability

While a barrier between the blood and CNS exists, it stood to reason certain molecules are permitted to pass. If not, the CNS would be devoid of nutrients and thus dead. Studies in the 1940's and 50's confirmed that transfer of small molecules, nuclides, and nutrients across the BBB occurred (Manery and Bale, 1941; Katzman and Leiderman, 1953). The methods used in the different studies were similar, radioactive nuclides were injected into animals, and after a set duration of time, the animals were euthanized. Their CNS tissue was then analyzed using a Geiger counter which confirmed the presence of these radioactively tagged nuclides (Katzman and Leiderman, 1953).

Simultaneously, simple sugar diffusion was being analyzed as well; the two most used being glucose and fructose. An early study demonstrated that glucose appeared to diffuse with greater ease than fructose across the BBB (Klein, 1946). The study, however, was lacking – it failed to provide quantitative data upon the phenomenon. It did raise an interesting possibility though; according to the results the transport of glucose appeared to be facilitated across the normally impassable membrane. This observation was later confirmed by using radioactively labeled glucose. Blood was passed through the BBB with varying glucose concentrations and

the percentage removed in a single pass was calculated. The results showed that at high concentration around 10% glucose was removed, whereas with low glucose concentrations nearly 50% of it was removed. (Crone, 1965). These results are the foundation for the creation of [^{18}F]-FDG and current attempts to attach pharmaceuticals to glucose; a sort of trojan horse approach.

2.3) Nasal Passage

The first indication that a pathway to bypass the BBB existed was found in 1937 by William Faber. Working with rabbits, he administered a dye to the nostrils of the animals and then noticed that unlike previous studies, the dye had been transported into the central nervous system (Faber, 1937). At that time, however, the exact implications of his findings were unknown, and the discovery was largely ignored. It was not until medicine advanced further, that this pathway was further explored and exploited.

It would take until 1989 when William Frey II, specializing in Alzheimer's and neuroscience, discovered the intranasal (IN) administration route was suitable for human treatment (Frey, 1991). He found that therapeutic agents administered to the olfactory neuron region within the nasal cavity would result in neurologic effects taking place within the CNS. Immediately, Frey postulated many treatments which could be utilized in this manner; and in the following years his research proved them to be true. Some ailments include, but are not limited to, Alzheimer's disease, Parkinson's disease, and affective disorders (Frey, 1991).

Interestingly, he also suggested that it could be used for radiopharmaceutical administration to aid in brain tumor discovery. This is a non-ubiquitous realization

because [^{18}F]FDG already existed. To this day, it remains the prominent radiation source for brain PET/CT scans; interest in IN administration for radiotracers did not arise for another two decades (Singh, 2018).

2.4) Review of Pharmaceuticals

A quantitative review of 73 publications ranging from 1970-2014 sought to analyze the delivery success of pharmaceuticals through standard and IN administration routes. It should be noted, there were two thousand more studies performed on IN administration during this time period; however, only those which matched the criteria that allowed for analysis were utilized (Kozlovskaya, 2014). The plethora of studies upon this topic stemmed from the realization that 100% of macromolecule drugs and 98% of small molecule drugs could not penetrate the BBB (Gae, 2013).

Two standards were used in Kozlovskava's (2014) analysis, percent drug targeting efficiency (% DTE), and nose-to-brain direct transport (% DTP). The primary indicator of effective IN administration is DTE. It compares the percentage of pharmaceutical in CNS tissue vs circulating blood for both IN and IV administration. A percentage over 100% indicates the administration is more effective through IN than IV (Kozlovskava, 2014).

The pharmaceuticals analyzed were grouped into three different formulations: gel, particle, and solution. Percent DTE was calculated from the available data for each pharmaceutical; and then geometric means of each formulation were calculated. With averages of 518%, 475%, and 370% respectively, the results were staggering (Kozlovskava, 2014).

2.5) Radiotracers

The transfer of nuclides across the IN route has been documented for some time. All the early studies for transport and diffusion used radioactive labels to measure amount transported. A prime example would be ^{125}I labeled interferon-B in rhesus monkeys. Interferon-B was tagged with ^{125}I to gauge its distribution throughout the monkeys CNS. The tagged molecule was then administered intranasally and later found that it had indeed crossed via the neurons in the olfactory region (Thorne, 2008).

Accidental brain exposure to radionuclides can occur through the olfactory neurons as well. In 2014 it was proven that nasal inhalation of aerosolized uranium will result in uranium atoms being transported through the olfactory neurons into the brain (Chrystelle, 2014). This would be a concern to the public as well due to their frequent inhalation of radioactive particles such as radon.

Recently, a team attempted to quantify the difference in brain uptake between IN and IV administration of [^{18}F]FDG and [^{18}F]Fallypride (Singh, 2018). The findings indicated that IV administration is overwhelmingly more efficient for [^{18}F]FDG, and slightly more so for [^{18}F]Fallypride. In contrast, however, an earlier study could provide explanation for some discrepancy. In primates, it was found that when [^{18}F]FDG was targeted to the superior nasal conchae, instead of being applied universally, it would result in a 400% increase of brain uptake (Cross, 2011). These results are supported by another study in pharmaceutical science. It indicated greatly increased transport when the applied pharmaceutical was both targeted and immobile after application (Kozlovskava, 2014). If such a large increase in transport were

assumed, then the Singh study may have in fact proved IN administration competitive rather than obsolete. That study also attempted to estimate localized tissue dose through a dosing factor and hand calculation. The calculation, however, is a worst case scenario and assumes that particles are fixed within the nasal cavity. This leads to a harsh overestimate of dose. To illustrate this, Singh (2018) calculated 200 MBq would result in a 3 Sv dose to the skin of the nasal cavity. With the IN administration of [^{18}F]Fallypride appearing to be highly competitive, further work into the dosimetry was warranted. Additionally, [^{18}F]FDG transport appears to be highly affected by administration procedure. If adjustments were made and the transport tested again, it too may prove to be competitive.

3) Background

3.1) Advantages of Intranasal Administration

While it carries the additional risk of a localized dose, intranasal administration does potentially offer two advantages over intravenous. First, by providing a direct route to the brain, it allows for a greater array of radionuclides to be used (Frey, 1991). Currently, only those which can bypass the blood brain barrier are candidates for brain imaging (Singh, 2018). Secondly, intranasal administration has the potential to be better targeted directly to the brain – meaning that less total activity may be required for successful imaging (Singh, 2018).

As is true with pharmaceuticals, the intranasal pathway provides an unfettered delivery route for radionuclides. This route is actively used to deliver large macromolecules which could not ordinarily be used to treat CNS diseases

(Kozlovskaya, 2014). While the application for the pharmaceutical industry is clear, the relation to medical imaging is slightly less conspicuous. Each radiotracer comes with a set of characteristics, including advantages and disadvantages (Singh, 2018). Because of the BBB, brain imaging is currently restricted to a small pool of radiotracers (Frey, 1991). By allowing direct access, the restriction upon radiotracers is lifted, granting a much wider selection depending on what the situation needs.

The second advantage is more theoretical and requires further testing to confirm. By applying the radiotracer in a region with direct access to the brain, technicians seek to circumvent the greatest disadvantage of intravenous administration – whole body circulation (Singh, 2018). When a radiotracer solution is administered intravenously it is rapidly circulated throughout the entire body (Chaly, 2010). Since the radiotracer is attached to glucose, virtually every tissue in the body has an affinity for it. This leads to widespread distribution and a heavy dose to certain organs such as the bladder or kidneys (Chaly, 2010).

Conversely, intranasal transport has a direct route to the brain – making it possible to target the radiotracer to the brain, reducing the amount of circulation. This could lower the whole-body dose to the patient and simultaneously reduce the total amount of activity required for imaging. With a direct path and targeted delivery, it also stands to reason that transport to the brain may be more efficient than with IV administration; this has proven to be the case for many pharmaceutical drugs (Kozlovskaya, 2014). Because of more efficient transport, less total pharmaceutical is required per treatment compared to IV administration (Kozlovskaya, 2014). This

same concept can be applied to medical imaging, better transport means less initial activity required to reach sufficient levels for image clarity (Singh, 2018).

3.2) Anatomy

The nasal cavity consists of three regions, the vestibule, respiratory region, and olfactory region. Figure 1 provides a breakdown of the regions within the nasal cavity.

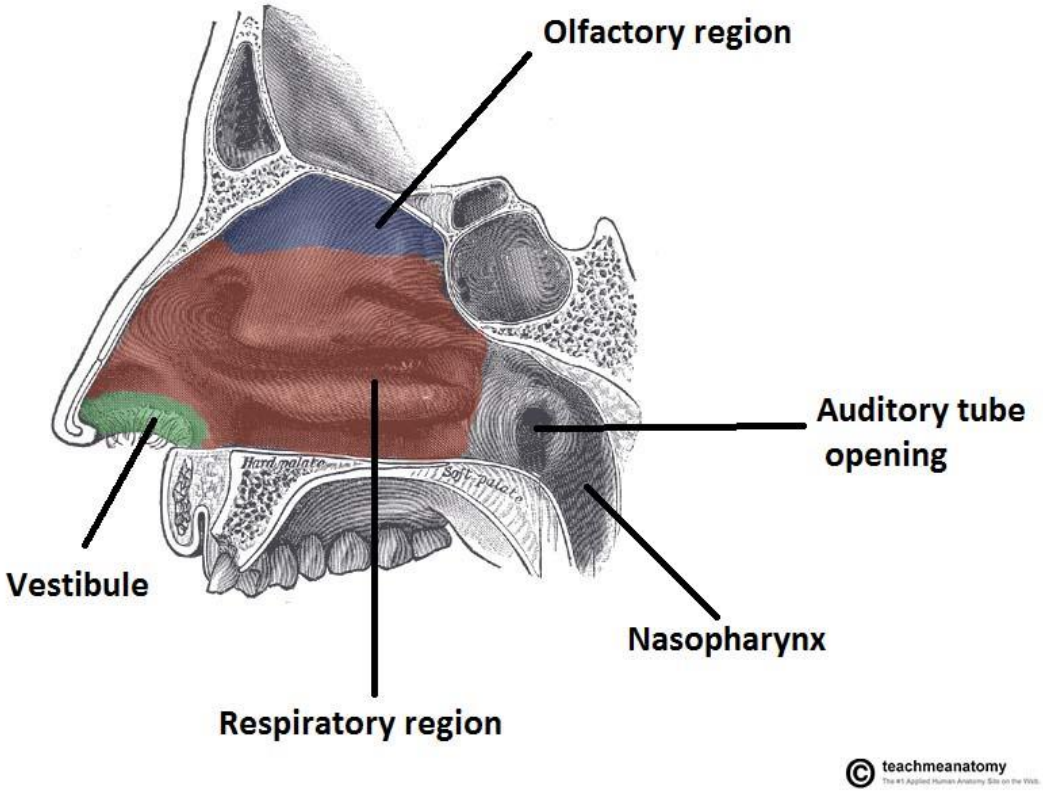

(TeachMe, 2020)

Figure 1: Sagittal View of Nasal Cavity

The vestibule, noted in green in Figure 1, is the area immediately surrounding the opening of the nasal cavity. Its purpose is the filtering of air and entrapment of

larger airborne particles that may be present (Sobiesk, 2019). It serves no purpose in the application of intranasal administration and can largely be ignored (Gizurarson, 2012).

Moving inward, the next region encountered is the largest of the nasal cavity; denoted in red, this is the respiratory region. Primary functions include filtering, warming, and humidification of inhaled air (Sobiesk, 2019). Warming and humidification are both accomplished by the neuurovascular system. The interior of the nasal cavity has an extensive blood supply with many arteries and vessels running proximal to the interior surface (Gizurarson, 2012).

To maximize surface area and thus contact with incoming air, there are three folds within the respiratory region (Sobiesk, 2019). Referred to as nasal conchae, they occupy most the volume of the nasal cavity and provide smaller channels for the air to pass through. Blood flow is continuously regulated to these conchae and adjusted via a feedback system based upon airflow (Sobiesk, 2019). Figure 2 illustrates a coronal slice of the nasal cavity and the channels that they produce. These channels account for the majority of the surface area within the cavity; approximately 96% is directly attributed to the respiratory region (Gizurarson, 2012).

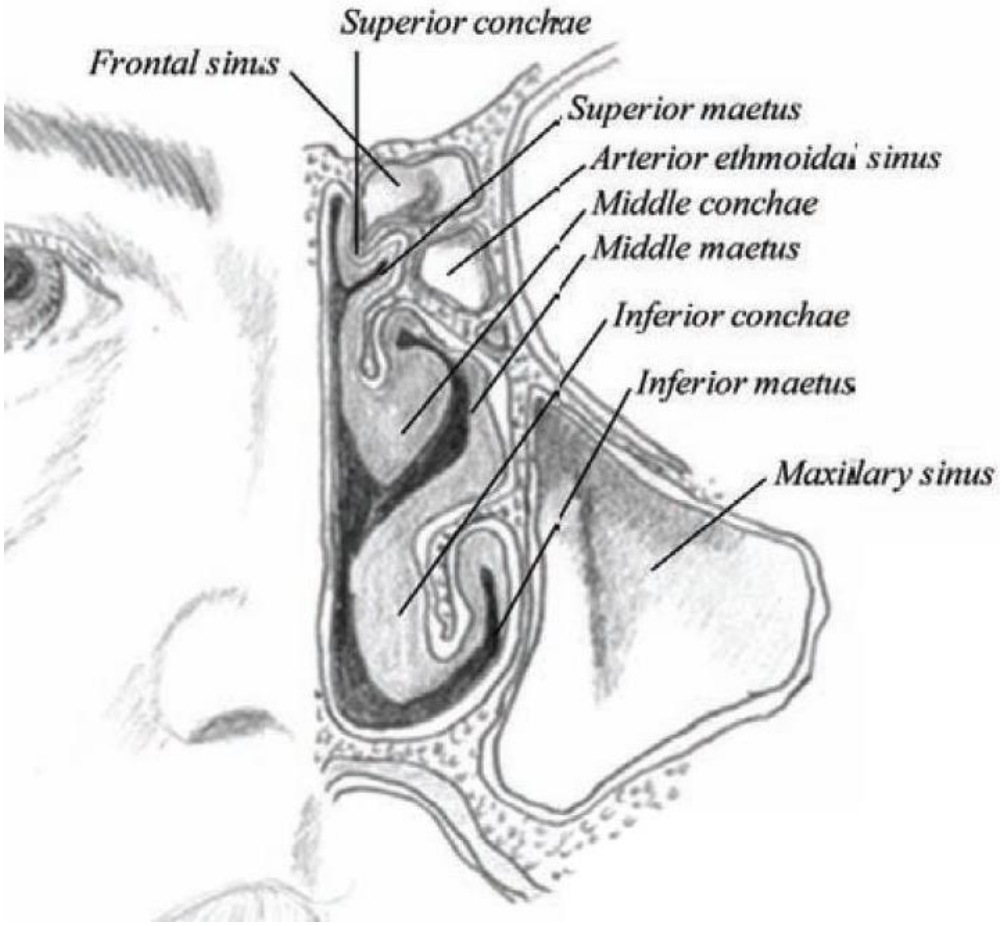

(Gizurarson, 2012)

Figure 2: Coronal View of Nasal Cavity

The final function of the respiratory region is the filtering of air. This region relies upon sticky mucosa to trap particles which pass by the vestibule. Once entrapped, cilia embedded in the epithelium tissue begin to sweep the particles towards the nasopharynx for removal (Sobiesk, 2019). This transport of foreign particles also applies to radioligands; the body will naturally remove them from the nasal cavity. The rate of transportation is not inconsequential as the cilia are capable of moving mucosa up to one centimeter per minute (Sobiesk, 2019).

Superior to the respiratory region resides the final portion of the nasal cavity – the olfactory region (Gizurarson, 2012). Indicated by blue in Figure 1, the olfactory region is located at the apex of the nasal cavity. Primary function of this region is to provide sense of smell - it accomplishes this through the olfactory nerve. This nerve penetrates the cribriform plate separating the nasal cavity from the brain (Samaridou, 2017).

When all three regions are combined and inner folds are accounted for, the internal surface area of the nasal cavity is 160 cm^2 (Gizurarson, 2012). As mentioned previously, the respiratory region accounts for 96%, or 153 cm^2, of this area. The vestibule comprises 0.6 cm^2 and can largely be ignored, the remaining area composes the olfactory region. This region varies depending on the individual, but is generally accepted to be between 5 and 8 cm^2 (Gizurarson, 2012). Additionally, it needs to be noted that the nasal cavity is split down the middle by the septum. The septum is essentially a wall of cartilage and is typically bent towards one side or the other – the two nasal cavities are often not the same size (Gizurarson, 2012).

3.3) Transport Mechanism

While the exact mechanics are disputed, there are currently three leading theories (Samaridou 2017):

1) Axonal transport following internalization of the pharmaceutical;
2) Paracellular transport across gaps between cells, particularly those lining the olfactory neurons; and
3) Transcellular transport across basal epithelial cells.

Axonal transport occurs via two main nerve clusters, the olfactory and trigeminal. Being the largest cranial nerve, it has been found that the trigeminal pathway delivers a substantial amount of administered substance to the CNS (Samaridou, 2017). Unfortunately, the rate at which it does so is not useful to radionuclide administration. Transport via this nerve can take several hours to complete, by the time delivery occurs, most current radiotracers would have decayed through several half-lives and would no longer be useful for imaging (Samaridou, 2017).

Animal studies, however, have found significant concentrations of administered agents in brain tissue 30 minutes after application (Samaridou, 2017). Due to the time frame, this indicates that axonal transport cannot be the only method of transmission. Rather, a more direct route would be required to facilitate rapid transport. The only option which fits the criteria is paracellular transport along cell gaps. These gaps provide direct access to brain tissue, making this theory the most relevant for radiotracers which are heavily time dependent (Samaridou, 2017). The gaps are most prominent among the cells which line olfactory neurons. Given the extent to which the olfactory neurons penetrate the cribriform plate, there are plenty of channels available for transport. Figure 3 provides a visual representation.

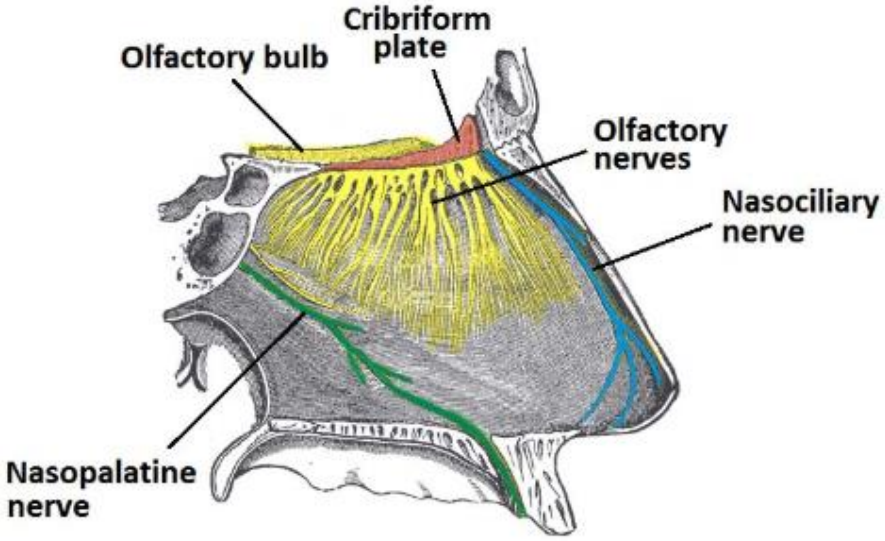

(TeachMe, 2020)

Figure 3: Innervation of Nasal Cavity

Olfactory neurons have a very important characteristic – they are in a state of constant regeneration (Liu, 2019). Immature olfactory cells take up less volume than their mature counterparts; the gaps are designed for mature cells. Because of this, the gaps they are supposed to fill are not typically sealed uniformly and permit transport (Liu, 2019). Due to this nature of diffusion-based transport, placement of the substance is very important. Mittal (2014) has demonstrated that even head positioning can affect the uptake of substance to the CNS. By tipping the patients head forward and utilizing gravity to hold the applied substance in the olfactory region, better transport ratios are achieved (Gizurarson, 2012). Additionally, in the case of radionuclides, this would lower the whole-body dose to the patient as it would prevent some loss of radionuclide via the nasotracheal exit.

3.4) PET/CT Scan

This form of imaging utilizes positrons as the primary emission source. Doing so gives a specific advantage, greater sensitivity than any other type of medical imaging (Schmitz, 2013). Because of this, less radiotracer is required for the procedure which minimizes radiation exposure and risk to the patients. One of the ways PET/CT scans accomplish this is through the use of coincidence.

When positrons annihilate, they release photons in opposite directions. By recreating the vectors traveled by these photons a singular ray can be drawn to their point of creation. The detectors utilized in PET scans are set up in a large ring formation to do just that (Strunk, 2018). When opposing photons are recorded within a certain time-period, generally a few nanoseconds, and within acceptable limits for geometric angle, it is considered a coincidence event (Shultis, 2007).

Upon the verification of a coincidence, a line of response is created connecting the regions of the detector which registered the photons – the point of creation lays upon this line (Strunk, 2018). After enough lines of response have been created, the location where they intersect most frequently indicates the highest level of activity.

This is particularly useful for imaging tumors. Cancerous cells have a higher metabolic rate due to one of their defining characteristics – uncontrolled growth and division. Doing so requires a higher than average glucose consumption. Using a tracer such as [^{18}F]FDG will result in a high concentration of ^{18}F in the tumor because it is attached to glucose for which the cancerous cells have a high affinity (Strunk, 2018). This results in an increase in decays occurring in the tumor and leads to more lines of response being drawn through that location.

4) THEORY

4.1) Positron Decay

Positron (or positive beta) decay occurs in proton rich nuclides. These nuclides typically transition by converting a proton into a neutron, releasing a positron and neutrino in the process. Much like negative beta decay, the energy of the released positron is not a fixed value, but rather a spectrum. The decay itself, however, releases a fixed amount of energy. If energy remains after the positron is created, it is then transferred to a neutrino. This neutrino is released by the nucleus, balancing the conservation of energy equations (Shultis, 2007).

Positrons share the same physical characteristics as electrons, however, have the opposite charge of +1. Because of their charge, the distance they travel is limited. Positrons constantly interact with electrons after their emission, resulting in an average path length of barely a couple millimeters in tissue (Shultis, 2007). At the end of its path, the positron undergoes an interaction with an election, annihilating and ending its existence (Shultis, 2007).

4.2) Annihilation Photons

When an electron and positron annihilate their energy must be conserved. Governed by Einstein's famous equation relating mass and energy $E=mc^2$, the rest masses of the particles are converted into energy. This energy takes the form of two photons, each having 0.511 MeV of energy. Another interesting facet to the annihilation and production is that the photons are emitted in nearly opposite directions from each other (Schmitz, 2013). Figure 4 indicates they are separated by exactly 180 degrees; however, this is often not the case. Small amounts of kinetic energy are carried into the

annihilation, this energy is conserved and expressed through variation in emission angle. These variations are very small and only tend to be a fraction of a degree (Shultis, 2007). Reason being the particles will not annihilate until they have expended nearly all their energy. Additionally, the small amount of energy left over is only expressed via emission angle, it will not be transferred into the photons – they are always 0.511 MeV (Shultis, 2007).

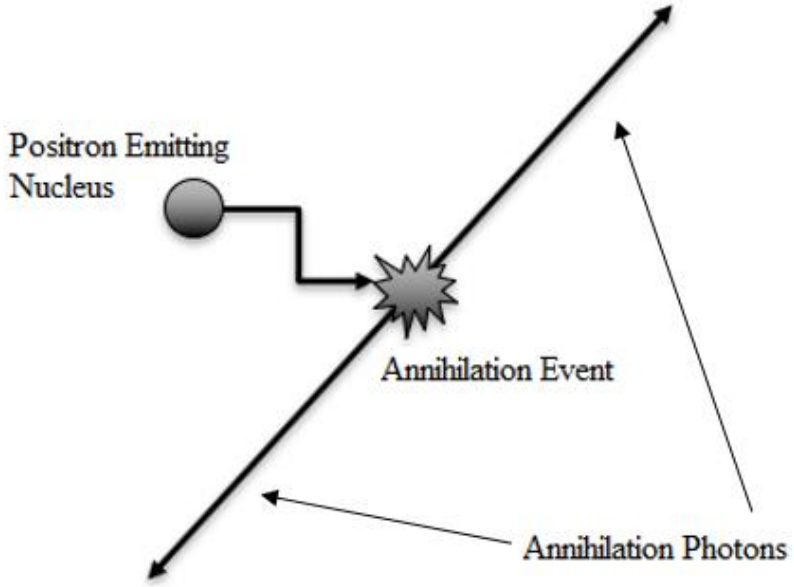

Figure 4: Annihilation Photon Production

4.3) Beta Particle Interactions

Both positive and negative beta particles interact in a very similar manner. There are very minute differences, however, current MCNP models uses the same transport physics (MCNP Manual). Equations which govern beta minus (electron) interactions are assumed to also be accurate for positrons. For this reason, these two particles are to be treated as interchangeable for this section.

Beta interactions differ from neutral particles because they do not require a physical impact to transfer energy. Due to their charge, they interact Coulombically, constantly slowing and depositing energy proportional to their stopping power. This causes charged particles to have a much shorter range than neutral particles, and constant interaction forces them on a torturous path (Shultis, 2007).

Interactions occur frequently and early in the beta particles' existence. At 60% of their total penetration distance, electrons have already released 80% of their energy (Martin, 2013). Typically, dose will be higher closer to the surface. Though, as with photons, there is a buildup region. However, the electron depth-dose curve starts around 85% of maximum dose and peaks much sooner (Martin, 2013).

Beta dose relies on particle flux, stopping power, and quality factor. Stopping power is the measurement of average energy loss per unit distance traveled. It is not a fixed value and is heavily reliant upon speed of the particle, charge of particle, and density of medium (Tsoulfanidis, 2011). If any of these factors are changed, the stopping power changes as well – it is not a fixed value for any particle.

The dose rate at any particular depth can be estimated using the following equation. It combines particle energy flux (E), stopping power (dE/dx), quality factor for particles of energy E (Q(E)), and density of medium (ρ) (Tsoulfanidis, 2011).

$$H = (E)\left[\frac{particles}{m^2 s}\right]\left(\frac{dE}{dx}\right)\left[\frac{MeV}{m\ part.}\right]\left(\frac{Q(E)}{\rho}\right)\left[\frac{m^3}{kg}\right]$$

There are two primary forms of beta interaction which contribute to dose: direct ionization and radiative energy loss – also known as bremsstrahlung (Martin, 2013). Direct ionization occurs between two electrons. The kinetic energy of the free beta particle is such that the Coulombic forces between it and an orbital electron can cause the orbital electron to eject (Tsoulfanidis, 2011). This process requires a fixed amount of energy dependent on the binding energy of the medium, and the result is the production of an ion pair (Martin, 2013). The energy required to eject the electron is absorbed by the respective nucleus, imparting dose into the medium. If a high energy beta particle collides with an inner shell electron, it has the potential to eject it. If ejected, the atom will then release characteristic X rays as the vacancy in the inner shell is filled; these too are absorbed locally (Martin, 2013).

The other dominant form of interaction is radiative, commonly called braking radiation or bremsstrahlung (Tsoulfanidis, 2011). It occurs when an electron is accelerated or decelerated by Coulombic forces from electrons or nuclei (Tsoulfanidis, 2011). This directs the electron on a new path and forces it to give up kinetic energy in the process. The kinetic energy lost is released as bremsstrahlung photons which are created with an energy equal to the amount lost by the electron (Tsoulfanidis, 2011). This process is driven by the Z of the medium, higher Z materials will result in much greater forces and produce more bremsstrahlung (Martin, 2013).

4.4) Photon Interactions

Photons are a quantum particle with no charge and zero rest mass. They travel at the speed of light and have an energy of $\mathbf{E=h\nu}$ (Tsoulfanidis, 2011). Where h is Planck's constant and ν is photon frequency. These particles interact in three

predominant mechanisms with probabilities dependent on their respective energy. With the source nuclide of ^{18}F only two mechanisms, photoelectric and Compton scattering, are possible; the energy of released photons is not sufficient for pair production (Chaly, 2010).

Photoelectric effect occurs when the photon interacts with a bound inner-shell atomic electron. The photon is absorbed, and its entire energy imparted into the atom (Tsoulfanidis, 2011). This causes the ejection of an electron which is known as a photoelectron. Because of its relatively small mass the kinetic energy of the photoelectron is given by:

$$KE = E_y - B_e$$

where E_y is incident photon energy and B_e is binding energy of the affected electron. Virtually all interactions with lighter nuclei occur with k shell electrons (Tsoulfanidis, 2011). Photoelectric effect is dominant for lower energy photons and the probability of its occurrence decreases with increasing photon energy (Tsoulfanidis, 2011). A rough approximation of photoelectric cross section can be found using this equation:

$$\sigma_{ph} = \frac{Z^4}{E^3}$$

It demonstrates the two most important factors are Z of material and photon energy. Higher Z targets with lower energy photons result in the greatest chance of photoelectric effect occurring (Tsoulfanidis, 2011).

Compton scattering is an interaction which occurs between a photon and outer-shell or free electrons. It typically dominates the energy range from a couple hundred

keV up to several MeV, where pair production takes over (Shultis, 2007) Even though outer shell electrons are bound, these interactions can occur due to energy difference. When the energy of the photon is in the order of keV or higher, and the electrons binding energy in eV, it is considered a free electron from the perspective of the photon (Tsoulfanidis, 2011).

Unlike photoelectric effect, photons are not eliminated after a Compton interaction. The interacting electrons are incapable of absorbing all the photon's energy (Tsoulfanidis, 2011). Instead, the photon is scattered off the electron, imparting part of its energy and changing direction of travel. The scattered photon energy is calculated with the following equation:

$$E_{y'} = \frac{E_y}{1 + (1 - cos\theta)(\frac{E_y}{mc^2})}$$

E_y is incident photon energy, cosϴ is angle of scatter, and mc^2 refers to the rest mass of the Compton electron.

Using the conservation of energy law, energy imparted is the difference between initial and final photon energy.

$$E_{imp} = E_y - E_{y'}$$

Because photons are not destroyed after a Compton scatter, they can undergo many Compton interactions. Depending on the angle of scattering, each will remove a portion of the photons' energy until it undergoes photoelectric effect and its energy is completely absorbed (Tsoulfanidis, 2011).

5) MODEL DESIGN

5.1) Full Distribution Design

During creation of this model there were three key concerns which needed to be addressed:

1. Surface area must accurately reflect the accepted value of 160 cm^2;
2. Geometric structure must be like that of actual nasal cavity such that radiation interactions are not lost due to oversimplification; and
3. Basal cell depth for interior nasal cavity membrane is 20 microns.

Accommodating the surface area was not an overly complex task. Many different structures could be utilized while maintaining the required area, however, one assumption was made while considering this aspect of the model. Instead of modeling the three separate regions of the nasal cavity, it was instead assumed that the dose values would not vary significantly if the respiratory region were enlarged to encompass the entirety of the 160 cm^2.

This assumption was valid for two reasons: the respiratory region accounts for 96% of the total surface area, and the tissue composition between the two internal regions, respiratory and olfactory, does not vary (Jafek, 1983). It has been noted that the tissue of the vestibule (opening of the nasal cavity) is more callous than the interior. It is comprised of a different structure than the other two regions, however, the vestibule composes 0.6 cm^2 of the total surface area and is located at the entrance of the nasal cavity. Due to its small surface area and location which will not be affected by radioligand administration, it was discounted. Instead, the surface area was added

back into the model with respiratory epithelium assumed. This would result in a very slight overestimation of dose which is preferable to underestimation.

The final region, olfactory, encompasses the last five to six square centimeters. It shares the same tissue composition of the respiratory epithelium and sits at the apex of the respiratory region. Essentially, the olfactory region can be considered the roof of the nasal cavity. Attributing its surface area to the respiratory region made assigning dimensions to the model a much more straightforward task. Additionally, it also removed the need to model a secondary geometric structure for the olfactory region. By following this simplification of the interior regions, an anatomically accurate model was designed without unnecessary complication.

The geometry of the sinus model relied heavily upon the types of radiation involved. The two predominant sources of radiation within the model were positrons and subsequent annihilation photons. Positrons, by nature, have a low penetration range and quickly deposit their energy – they will not deliver dose far from their point of creation. Annihilation photons, however, travel much farther and can deposit energy over a greater distance. Because of this, internal structure becomes more important – if positrons were the only source considered, then a simplistic model with matching surface area would have sufficed. Additionally, annihilation photons are created with an energy of 0.511 MeV – interactions at this energy level tend to be dominated by the Compton effect. Every interaction will influence the direction of the photon; thus, it was important to keep the region of interest anatomically accurate as to allow interactions to scatter photons back into the internal structures.

The inner structures of the model were created using a standardized geometry developed by a collaboration between the Carleton University and Ottawa Civic Hospital (Liu 2009). This team combined CT scans and digital 3D modeling which resulted in an excellent view of the channels within the nasal cavity. Figure 5 provides a sagittal and coronal view of the internal structure.

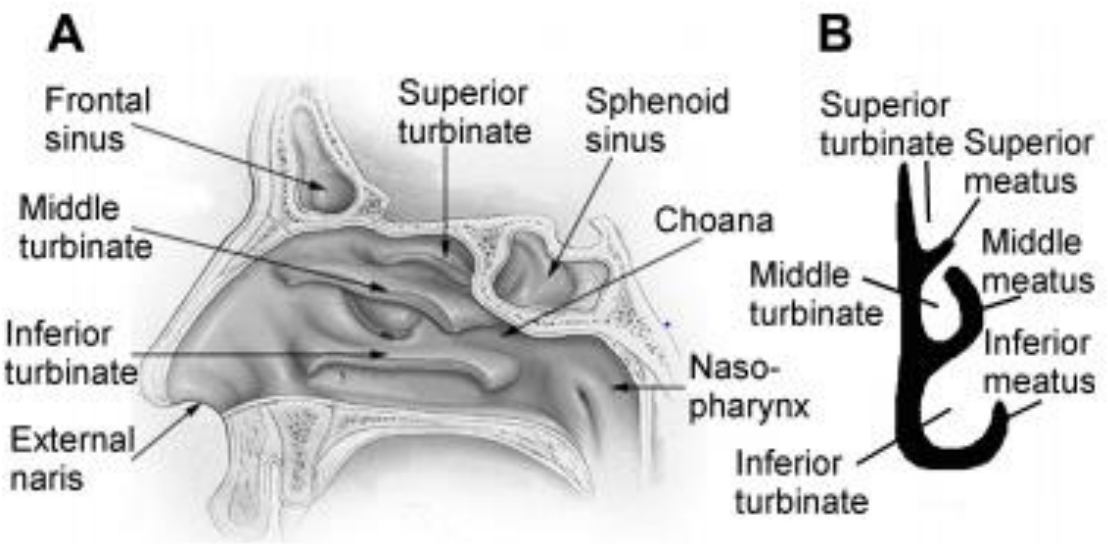

(Liu, 2009)

Figure 5: Sagittal and Coronal View of Nasal Passage

As seen in the coronal view of Figure 5, the turbinates form three separate channels through which air can pass. More importantly, these turbinates create multiple different surfaces for interactions. Photons can travel through the couple centimeters of tissue which comprise the turbinates and interact at each layer of basal cells. Within the model these same opportunities for interaction had to be present. The model is slightly more rigid, however, encompassing the shape and number of points of interaction. The

first portion of the model designed was the right nasal cavity. Figure 6 compares the rendered image with a replication of the model.

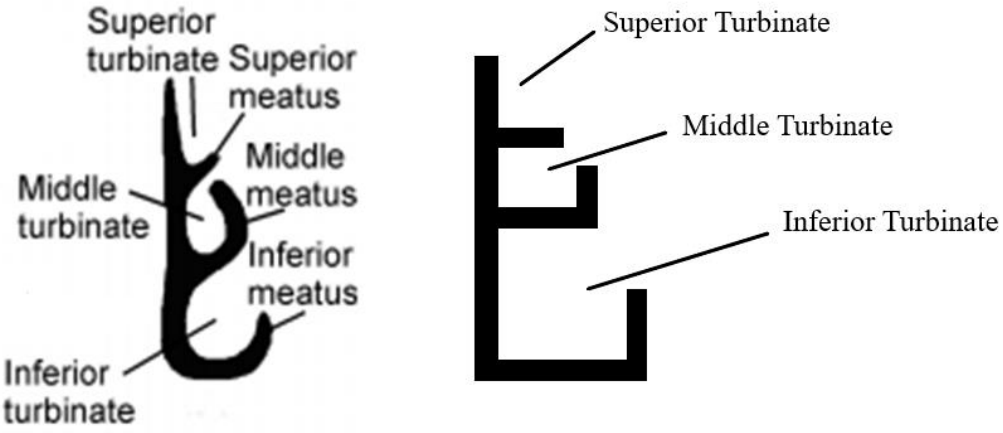

Figure 6: Coronal View of Nasal Passage vs Model

The regions denoted in black represent the three separate meatus which comprise the passageway through the nasal cavity. The goal was to replicate the structure while remaining within the constraints of MCNP. For this reason, the meatus in the model did not follow the 3D rendering exactly, however, provided appropriate pathways for interaction and annihilation photon creation. With the right side of the model designed, creating the left nasal cavity was simply a task of mirroring the image. While irregularities do exist between sides of the nasal cavity, there is no pattern which allows for reproduction of these irregularities and thus, it is accepted that they may be considered symmetrical (Liu, 2009).

The final portion of the model to be considered was the septum wall. It is a thin wall comprised of cartilage and bone which divides the two sides of the nasal cavity –

typically two to three millimeters thick (Hwang, 2010). The thickness does vary a small amount depending on the region, however, in the model it was held constant. Figure 7 (not to scale) shows the completed model from a coronal view.

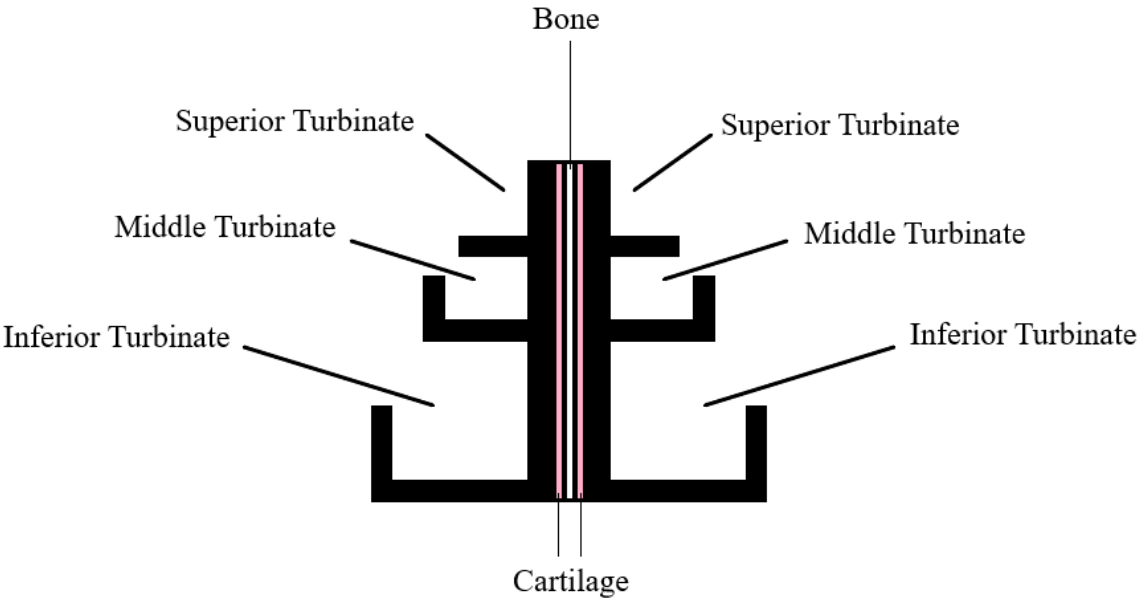

Figure 7: Coronal View of Model

Each slice of the septum was held at one-millimeter thickness, resulting in two millimeters of cartilage and one millimeter of bone through the center. This completes the inner structures of the nasal cavity and leaves one final point to address, basal cell depth.

Tissue dose is typically assessed at the depth where the basal cell layer is found. These are the cells responsible for creating new cells and are most vulnerable to radiation damage since they must replicate rapidly. Being an interior membrane, the basal cells of the nasal cavity are close to the surface. An evaluation of respiratory epithelium using electron microscopes confirmed this, basal cells were found between

20-30 micrometers depth (Jafek, 1983). This gives an idea of where to assess dose within the model, but not how.

The solution utilizes another set of MCNP cells which surround the entirety of the model – these will be referred to as dose cells. The dose cells have a height of 10 microns, which matches the 20-30 micron depth at which basal cells are found. Figure 8 provides a view of dose cells encasing the entirety of the nasal cavity.

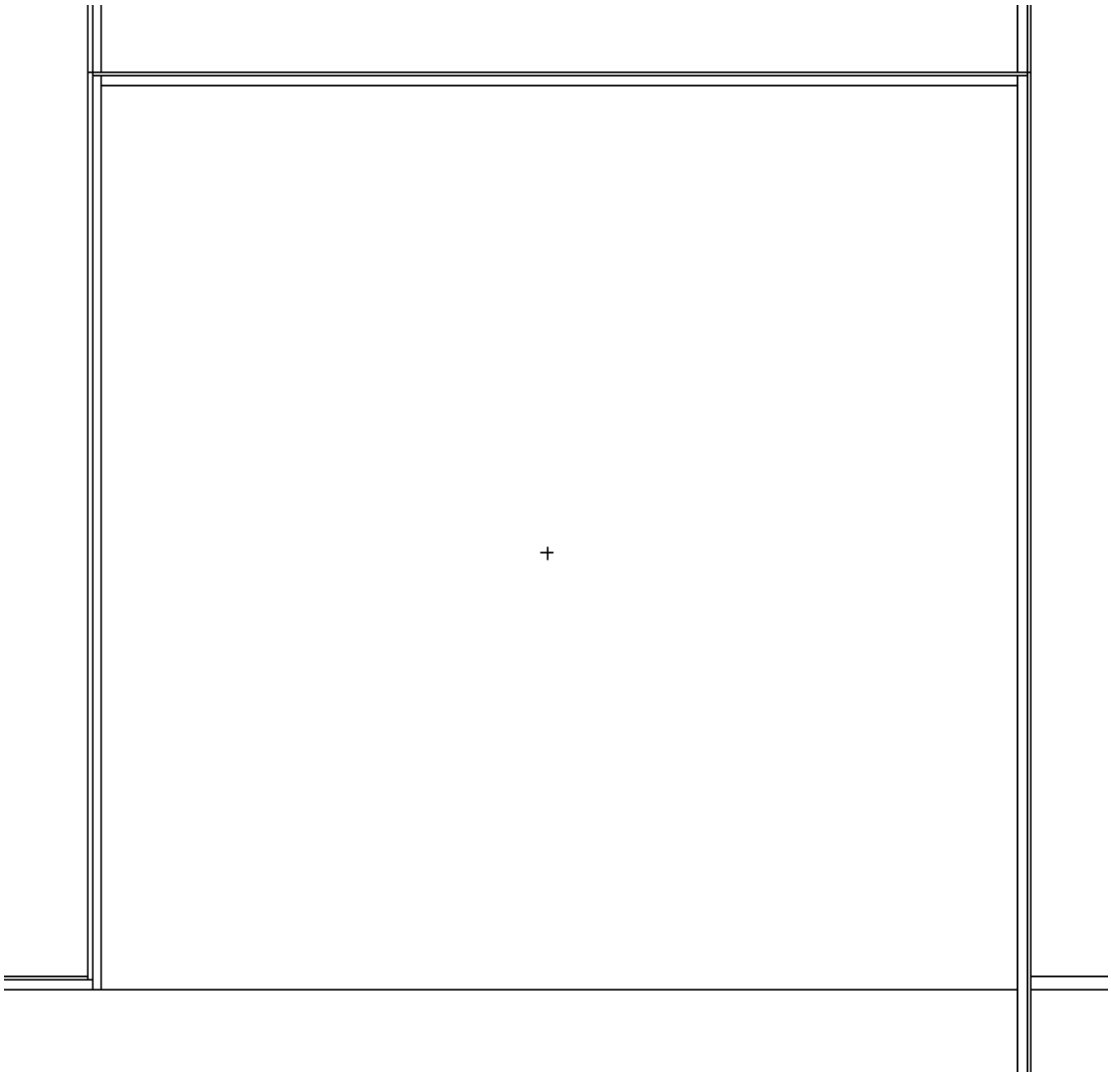

Figure 8: VisEd View of MCNP Dose Cells and Airway

Pictured is an enlarged vertical section of the air passageway formed by the nasal conchae. Looking at the left vertical wall, three distinct lines can be seen. The rightmost line represents the beginning of the respiratory epithelium. The area between the rightmost and middle line is called the depth plate or depth cell. There are 20 microns between the two lines and this area simultaneously serves as both the buildup region and positron shield until the dose region is reached. The middle and

leftmost lines section off the dose cell. Energy deposited within this region is calculated by MCNP, this value can then be transformed to dose. By ensuring that these dose cells cover the entire model, a very accurate tissue dose can be obtained. The completed model can be seen in Figure 9

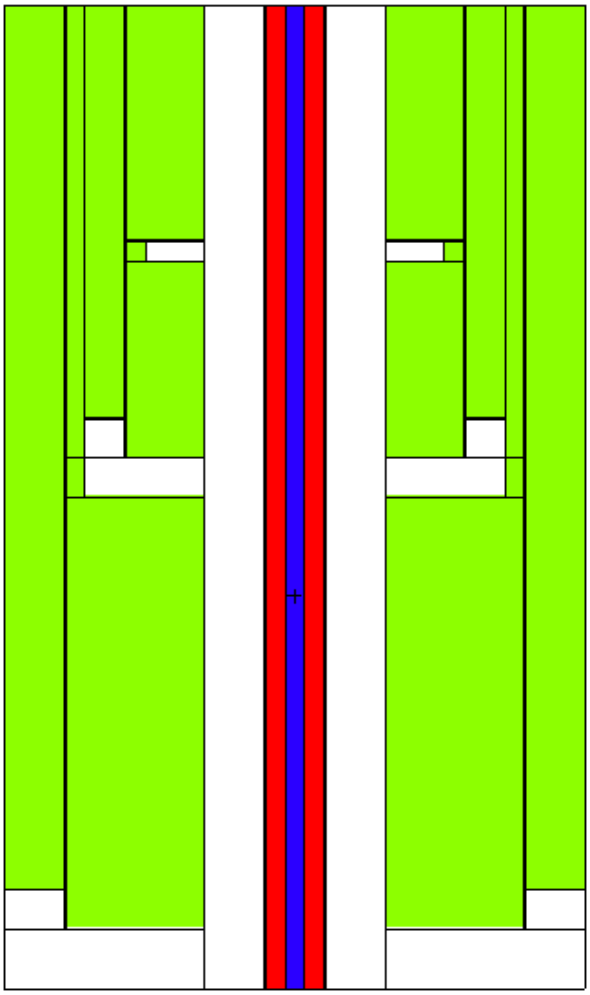

Figure 9: VisEd View of Full Distribution Model

This figure is colored by material, white is a void, or in this case airway, green equates to tissue, red is cartilage, and the dark blue is the bone slice. This is the model used for full deposition calculation. Source particles were distributed evenly throughout the vertical passageways to represent an inhalation of nasal spray.

5.2) Gel Distribution Model

One change was made to the original model to test gel distribution. This delivery form does not evenly spread throughout the nasal cavity, but rather is formulated to remain in place at the apex. The distribution within MCNP had to be changed to reflect this, Figure 10 provides an image of the solution.

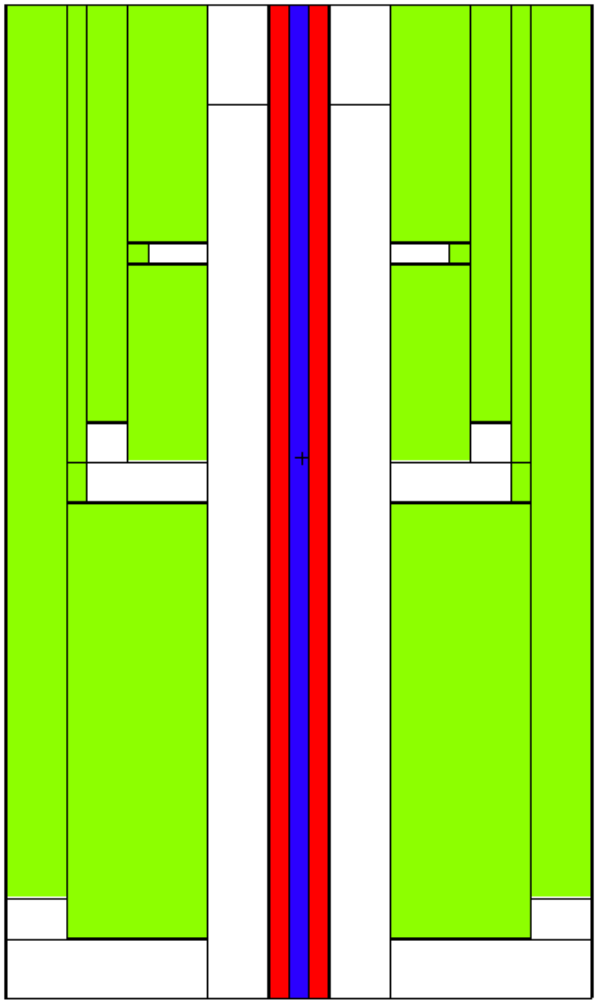

Figure 10: VisEd View of Gel Distribution Model

Another set of MCNP cells were created in the upper regions of the airways. They are marked by the line dividing the vertical sections adjacent to the septum wall. The cells extend down half a centimeter from the apex to account for slight migration of

the application gel due to gravity. By sectioning this area off, it allowed source particles to be concentrated within these cells and held against the apex. Two different doses can be calculated with this method, whole cavity, and local dose to the apex. The latter dose is relevant because of possible deterministic effects in which severe tissue damage may occur.

6) Methods

All simulations were built and run within MCNP 6.1. Visual editor was employed throughout the process to ensure no gaps in geometry. Energy deposition was found using an *F8 tally. This tally calculates total energy deposited within a cell (MeV) and returns the average value deposited per source particle. Since the value is calculated per source particle, it includes both the positron and annihilation photon dose. From this point, the data must be manipulated outside of MCNP to return a dose value.

A couple different conversions need to be made to convert to units of dose. The chosen unit of measurement is the Gray, Joules of absorbed energy per kilogram of mass. Since the value returned by MCNP is only a unit of energy, mass needs to be included. MCNP returns the mass of all dose cells in grams, dividing the MeV per source particle by this value will result in units of MeV/gram per positron.

$$\frac{MeV}{positron} \times \frac{1}{grams} = \frac{MeV}{g\ positron}$$

With units of energy per unit mass acquired, a conversion factor from MeV per gram to Joules per kilogram needs to be set up.

$$\left(1.602 \times 10^{-13} \frac{J}{MeV}\right) \times (1000 \frac{g}{kg}) = 1.602 \times 10^{-10} \frac{J\ g}{MeV\ kg}$$

Multiplying the MeV/g per positron by positron yield and the conversion factor is the last step to acquire Gray/disintegration.

$$\frac{MeV}{g\ positron} * \frac{0.97\ positrons}{dis} * 1.602\ \times 10^{-10} \frac{J\ g}{Mev\ kg} = \frac{J}{kg\ dis}$$

This value is then used to find both the initial dose rate, and total dose when activity is integrated over time. For the initial dose rate, the only step required is to multiply Gray/dis by activity, in units of dis/sec. To make an easy comparison to Varskin, this value was then multiplied by one MBq of activity and 3600s to convert to an hour.

$$\frac{Gy}{dis} \times \frac{dis}{sec} = \frac{Gy}{\mathrm{s}}$$

$$\frac{Gy}{\mathrm{dis}} \times \frac{10^6\ dis}{sec} \times \frac{3600s}{hour} = \frac{Gy}{MBq\ hour}$$

Total dose required a further step, activity had to be integrated over time. This gives the total number of decays which occur within the nasal cavity. That value is then

multiplied by the Gray/dis to return an estimate for total nasal cavity skin dose. Calculating it in this manner assumes the particles are fixed and that all decays would occur within the nasal cavity – this returns a worst-case scenario for dose. The activity used for this calculation is the lowest value recommended by the FDA for a PET scan, 185 MBq (Chaly, 2010).

$$D_t = D_r \int_o^T A\, e^{-\lambda t}\, dt = D_r\, A \frac{\left(1 - e^{-\lambda T}\right)}{\lambda}$$

Lastly, calculations were performed to generate expected error for the dose values. These were straightforward because MCNP itself returns the numbers required to calculate these intervals. The values for 95% confidence interval were selected, then processed in the exact same manner listed above. By comparing the range of these outputs to the original dose value, an expected range of error can then be determined.

7) Results

7.1) MCNP

Table 1 describes the whole cavity dose obtained from the models. These values were ascertained by combining all the dose cells into a single tally, which then averaged the energy deposited. Aside from full cavity distribution, three other tallies were taken from the gel distribution model – these can be seen in Table 2. The first tally is the dose at the cavity apex where the gel would be located. The dose cells

which are adjacent to the source particle distribution were tallied as a single unit. The second additional tally was the entire nasal cavity minus those dose cells used in the calculation for the apex. The third and final tally consisted only of the dose cells which surround the lower right airway.

Table 1: MCNP results from both models

Model	**Full Dist.**	**Gel Dist.**
Initial Dose (mGy/MBq/hr)	33±0.1	30±0.1
Total Dose (Gy/185 MBq)	16±0.05	15±0.05
Relative Error	1.65E-3	1.69E-3
Variance	2.07E-5	2.31E-5
NPS (Number of Particles)	1,000,000	1,000,000

Table 2: MCNP results from gel distribution model

Gel Model	**Cavity Apex**	**Whole w/o Apex**	**Lower Right Airway**
Initial Dose (mGy/MBq/hr)	252±1.3	9.5±0.07	0.27±0.02
Total Dose (Gy/185 MBq)	123±0.06	4.6±0.03	.13±0.01
Relative Error	2.58E-3	3.78E-3	0.032
Variance	3.98E-5	6.01E-5	.001
NPS	1,000,000	1,000,000	1,000,000

MCNP also calculates relative error and variance of the tallies. Each of these values is used to determine the validity of the results. Relative error is the expression of uncertainty within the mean. MCNP calculates it from the ratio of the standard deviation of the tally mean to the tally mean (Shultis, 2011). Table X gives the values needed to interpret the relative error returned by MCNP.

Table 3: MCNP relative error

Range of R	Quality of Tally
> 0.5	Meaningless
0.2 to 0.5	Factor of a Few
< 0.1	Reliable (Except for point/ring detectors)
< 0.05	Reliable even for point/ring detectors

The relative errors obtained during these simulations are significantly lower than the recommended values to assume data is reliable. Already this suggests the data is valid and can be used, however, variance also should be considered.

While relative error is an estimation of the tally's precision, variance is the estimation of the relative error's accuracy. It is possible to have an errant relative error which indicates bad results are acceptable. The MCNP manual recommends a value below 0.1 to assume the relative error is valid. The values returned for these simulations are within the accepted range for both relative error and variance; therefore, the results should be considered meaningful.

7.2) VARSKIN

In addition to the MCNP models, Varskin 6.2.1 was used to simulate energy deposition in the nasal cavity. Due to the constraint of 100 cm^2 as the maximum skin averaging area, it was not possible to model the entire cavity. Instead, the skin averaging area was set to 80 cm^2 – half the total surface area. Since dose is the amount of energy absorbed per mass, doubling the mass and energy absorbed by adding the second half of the cavity will result in the same value.

The source geometry chosen was slab, with side lengths of 8 and 10 centimeters. This results in an even distribution across the entirety of the skin averaging area. As with MCNP simulations, source activity was chosen to be one MBq and the time duration an hour. Lastly, skin depth needed to be set within Varskin. To match MCNP runs, 20 microns was chosen, and the simulations were executed. Figures 11 and 12 are screen captures of Varskin input and output tables, respectively.

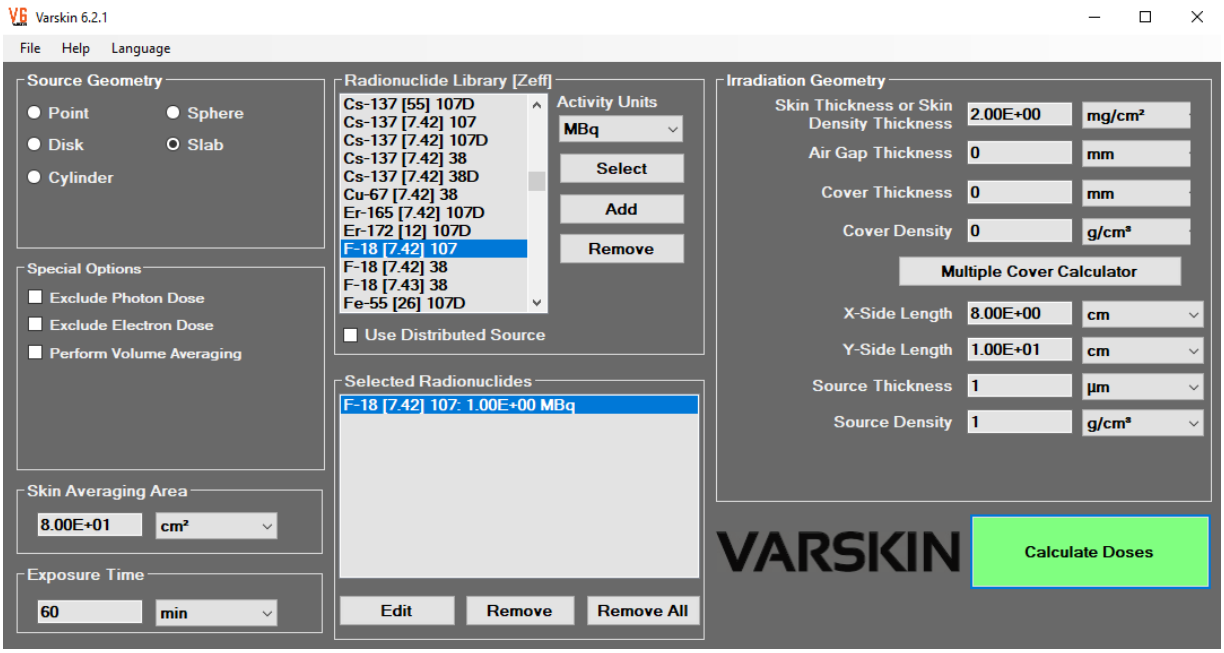

Figure 11: VARSKIN Input

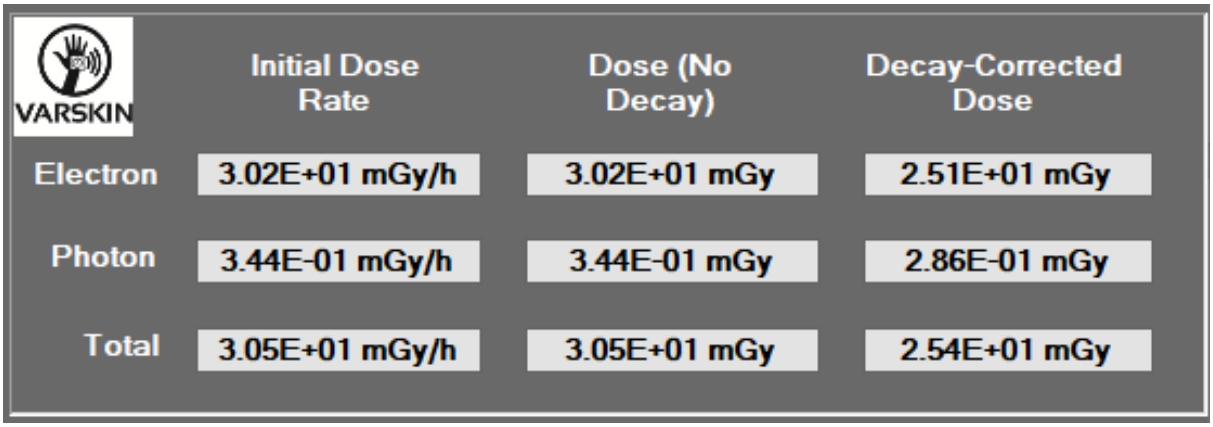

Figure 12: VARSKIN Output

8) Discussion

8.1) Full Distribution

Both Varskin and MCNP models provide similar dose estimates. MCNP simulations estimate dose 11% higher than Varskin. This is not entirely unexpected due to the geometry of the model within MCNP. There are more opportunities for particles to interact which would result in a slightly higher dose. Additionally, unlike a flat model, the corners of the meatus in MCNP provide opportunity to capture more than 50% of the positrons emitted. This is likely the biggest source of increased dose between the two models.

A typical PET/CT scan requires an intravenous injection of 185 to 370 MBq of radiotracer activity (Chaly, 2010). Assuming nasal transport is equally as effective as intravenous, the lowest possible injection would result in a dose rate of 6,290 mGy/hr. Calculating total dose with all particles fixed gives a potential dose of 16,000 mGy. Values this high have a severe risk of immediate skin damage. Exterior skin erythema begins around 2,000 mGy and the deleterious effects only increase as dose does, with skin necrosis beginning at 12,000 mGy (ICRP, 2000). There have also been reports of permanent olfactory neuron damage as a result of radiation damage (Bramerson, 2013). Patients receiving therapy to the head or neck region have been shown to have decreased sense of smell. In some cases, permanent loss of olfaction occurred (Bramerson, 2013).

8.2) Gel Distribution

The results from the gel model were far more nuanced than the full distribution. At the surface, the results between the two models appear to be fairly close, about an 8% drop from full distribution to gel. That, however, does not make sense when one considers that positrons are responsible for nearly all the skin dose. They simply do not have the range to irradiate the entire cavity to that extent. The culprit behind this misleading estimation are the methods used within the model.

When multiple cells are included in a single tally, MCNP averages the dose over those cells. Mathematically this is sound, however, if the cells are separated by a distance greater than particle range, logically it fails. In this simulation, the dose to the cells surrounding the "gel" is so high that it averages out to a significant whole cavity dose. The lower regions of the cavity should be receiving next to no dose because of positron range. To assess the extent of this effect required the addition of three separate tallies.

The first additional tally was to assess the local dose for skin touching the gel. It required dose cells to be segmented into gel and non-gel regions. With that accomplished, the cells adjacent to the gel were tallied separately. This tally resulted in a dose of 262 mGy/MBq/hr to the apex of the nasal cavity. As expected, this region experienced a massive energy deposition due to the positrons being so condensed.

Next, the cavity minus the cells used in the previous tally were averaged. This resulted in a whole cavity (sans apex) dose of 9.83 mGy/MBq/hr. This proves the apex dose severely skews the results of all other regions of the cavity. The extent, however, is not fully known because some of the dose cells used for this cavity tally

are touching dose cells used for the apex. They too, will skew the results for lower ranges in the cavity. One final tally was performed to validate this assumption.

The last tally was of the lower right airway. Geometrically speaking, this is the region farthest from the source location, and thus an excellent choice to determine how much radiation permeates the cavity. The dose in this region of the cavity was rather low, it came in at 0.28 mGy/MBq/hr. Being several centimeters away from the source meant that very few positrons would reach these dose cells. As a result, the dose in this region is 0.1% of the apex. Yet, if the total cavity dose including apex was believed blindly, one would incorrectly label this region as heavily dosed as well. To accurately assess dose throughout the entirety of the nasal cavity with an isolated distribution would require extensive segmentation of the dose cells by height. Doing so, however, is well beyond the scope of this thesis because the apex dose alone invalidates this delivery method.

At 252 mGy/MBq/hr, the deterministic effects to the olfactory region of the nasal cavity would be disastrous. If the same assumption of lowest acceptable administration activity at 185 MBq is made once again, that alone would indicate a dose rate of 48,470 mGy/hr. Calculating the total dose indicates 123 Gy to the cavity apex. Regardless of how these two results are viewed, one thing remains certain, doses of this magnitude are unacceptable and gel distribution cannot be considered for human use.

9) Conclusion

Results from both MCNP and Varskin models raise significant concerns regarding the localized dose to the patient. In this case, it would appear IN administration would have many deleterious effects upon the patient. As such, IN administration cannot be recommended for human use.

While it may technically be possible to use nasal spray as an administration route, doing so would not be recommended based upon results from previous studies which demonstrate poor nose to brain transport (Singh, 2018). When compared to IV administration, not only does IN route impart more dose to the patient per administered activity, but it would also require a higher amount of initial radiation to obtain the same image quality (Singh, 2018). As it stands currently, [^{18}F]FDG transmits better across the BBB than it does through nose to brain transport.

Utilizing a gel administration or other kind of contained delivery vessel is not suitable for use with radiotracers. The concentrated activity would cause irreparable damage to any tissues it contacts or is in proximity with (ICRP, 2000). This delivery method is more fitting for substances which do not cause damage based upon increased concentration.

Currently, future work cannot be recommended on this delivery method. Until an IN delivery aid becomes successful, this method of transport inferior and the dose to patient is much too high. The only way this route becomes viable is by vastly increasing the percentage of transport from nose to brain. In the interim, more work should be done with IV administration to test techniques for increasing image quality and transport.

References

1. Bramerson A, Nyman J, Nordin S, Bende M. Olfactory loss after head and neck cancer radiation therapy. *Rhinology*. 2013;51(3):206-209. doi:10.4193/Rhin12.120

2. Chaly, T. (2010). Fluorodeoxyglucose F 18 Injection. In NDA 21-870 (pp. 4-17). Beltsville, MD: Food and Drug Administration. Doi: https://www.accessdata.fda.gov/drugsatfda_docs/label/2005/021870lbl.pdf

3. CRONE, C. (1965) FACILITATED TRANSFER OF GLUCOSE FROM BLOOD INTO BRAIN TISSUE. J. Physiol. 181, pp. 103-113

4. CRONE, C. (1965). The permeability of brain capillaries to non-electrolytes. Acta physiol. Scand. (In the Press.)

5. Cross D, et al. Targeted Intra-nasal Delivery of Imaging Tracers and Therapeutics to the Brain: PET and MRI Investigations. *Conference: Radiological Society of North America*. 2011, print.

6. Davson, H. & Spazranii, E. (1959). The blood-brain barrier and the extracellular space of the brain. J. Physiol. 149, 135-143.

7. Deepti Mittal, Asgar Ali, Shadab Md, Sanjula Baboota, Jasjeet K. Sahni & Javed Ali (2014) Insights into direct nose to brain delivery: current status and future perspective, Drug Delivery, 21:2, 75-86, DOI: 10.3109/10717544.2013.838713

8. Delacroix et al, Radiation Protection Dosimetry - Radionuclide and Radiation Protection Data Handbook (Kent, England: Nuclear Technology Publishing, 1998), p. 24

9. Ehrlich P. 1885. Das Sauerstoff-Bedurfnis des Organismus: eine farbenanalytische Studie. Berlin: Hirschward.

10. Freiherr J, Hallschmid M, Frey WH, Brünner YF, Chapman CD, Hölscher C, et al. Intra-nasal insulin as a treatment for Alzheimer's disease: a review of basic research andclinical evidence. CNS Drugs 2013;27:505–14. https://doi.org/10.1007/s40263-013-0076-8.

11. Gizurarson S. (2012). Anatomical and histological factors affecting intranasal drug and vaccine delivery. *Current drug delivery*, *9*(6), 566–582. https://doi.org/10.2174/156720112803529828

12. Gizurarson, S. (2012, November). [Coronal View of Nasal Cavity]. Retrieved March, 2020, from https://www.ncbi.nlm.nih.gov/pmc/articles/PMC3480721/

13. H. Gao, Z. Pang, X. Jiang Targeted delivery of nano-therapeutics for major disorders of the central nervous system Pharm. Res., 30 (2013), pp. 2485-2498

14. Hwang K., Huan F., Kim D. J. Mapping thickness of nasal septal cartilage. *Journal of Craniofacial Surgery*. 2010;21(1):243–244. doi: 10.1097/SCS.0b013e3181c5a203

15. Ibanez C, Suhard D, Tessier C, et al. Intranasal exposure to uranium results in direct transfer to the brain along olfactory nerve bundles. *Neuropathology & Applied Neurobiology*. 2014;40(4):477-488. Doi:10.1111/nan.12061

16. ICRP, 2000. Avoidance of Radiation Injuries from Medical Interventional Procedures. ICRP Publication 85. Ann. ICRP 30 (2).

17. ICRP, 2007. The 2007 Recommendations of the International Commission on Radiological Protection. ICRP Publication 103. Ann. ICRP 37 (2-4)

18. Maynard, E. A., Schultz, R. L. & Pease, D. C. (1957). Electron microscopy of the vascular bed of rat cerebral cortex Amer. J. Anat. 100, 409-433.

19. Jafek, B. (1983). Ultrastructure of Human Nasal Mucosa. *Laryngoscope, 93*, 1576-1599. doi:10.1288/00005537-198312000-00011

20. Jones, O. (2019, September 29). The Nasal Cavity. Retrieved April 23, 2020, from https://teachmeanatomy.info/head/organs/the-nose/nasal-cavity/

21. KATZMANN, R. & LEIDERMANN, P. H. (1953). Brain potassium exchange in normal adult and immature rats. Amer. J. Physiol. 175, 263-270.

22. Lewandowsky M. 1900. Zur Lehre der Zerebrospinalflussigkeit. Z Klin Med 40: 480 –484.

23. Liu, Y., Johnson, M. R., Matida, E. A., Kherani, S., & Marsan, J. (2009). Creation of a standardized geometry of the human nasal cavity. *Journal of Applied Physiology, 106*(3), 784-795. doi:10.1152/japplphysiol.90376.2008

24. Liu, Y. (2009, January 1). [Sagittal and Coronal View of Nasal Passage]. Retrieved March, 2020, from https://journals.physiology.org/doi/pdf/10.1152/japplphysiol.90376.2008

25. MANERY, J. F. & BALE, W. F. (1941). The penetration of radioactive sodium and phosphorous into the extra- and intracellular phases of tissues. Amer. J. Physiol. 132, 215-231

26. Martin, J. E. (2013). Physics for Radiation Protection (Third). Weinheim, Germany: Wiley-VCH Verlag & Co. KGaA.

27. Maynard, E. A., Schultz, R. L. & Pease, D. C. (1957). Electron microscopy of the vascular bed of rat cerebral cortex Amer. J. Anat. 100, 409-433.

28. Miele, E., Spinelli, G. P., Tomao, F., Zullo, A., De Marinis, F., Pasciuti, G., Rossi, L., Zoratto, F., & Tomao, S. (2008). Positron Emission Tomography (PET) radiotracers in oncology--utility of 18F-Fluoro-deoxy-glucose (FDG)-PET in the management of patients with non-small-cell lung cancer (NSCLC). *Journal of experimental & clinical cancer research : CR*, *27*(1), 52. https://doi.org/10.1186/1756-9966-27-52 **

29. R. G. Thorne. DELIVERY OF INTERFERON-B TO THE MONKEY NERVOUS SYSTEM FOLLOWING INTRANASAL ADMINISTRATION. *Neuroscience* 152 (2008) 785–797

30. Samaridou, Eleni & Alonso, Maria. (2017). Nose-to-brain peptide delivery - The potential of nanotechnology. Bioorganic & Medicinal Chemistry. 26. 10.1016/j.bmc.2017.11.001.

31. Schmitz, R.E., Alessio, A.M., & Kinahan, P.E. (2013). The Physics of PET / CT scanners.

32. Shultis, J. K., & Faw, R. E. (2007). *Fundamentals of Nuclear Science and Engineering*. Boca Raton: CRC Press.

33. Shultis, K. (2011, December 12). An MCNP Primer. Retrieved April 5, 2020, from https://www.mne.k-state.edu/~jks/MCNPprmr.pdf

34. Singh N, Veronese M, O'Doherty J, et al. Assessing the feasibility of intranasal radiotracer administration for in brain PET imaging. *Nucl Med Biol*. 2018;66:32-39. doi:10.1016/j.nucmedbio.2018.08.005

35. Sobiesk JL, Munakomi S. Anatomy, Head and Neck, Nasal Cavity. [Updated 2019 Jun 26]. In: StatPearls [Internet]. Treasure Island (FL): StatPearls Publishing; 2020 Jan-. Available from: https://www.ncbi.nlm.nih.gov/books/NBK544232/

36. Strunk, A., Gazdovich, J., Redouté, O., Reverte, J. M., Shelley, S., & Todorova, V. (2018). Model PET Scan Activity. *The Physics Teacher*, *56*(5), 278–280. doi: 10.1119/1.5033868

37. T. (2020). [Innervation of Nasal Cavity]. Retrieved February, 2020, from https://teachmeanatomy.info/head/organs/the-nose/nasal-cavity/

38. T. (2020). [Sagittal View of Nasal Cavity]. Retrieved February, 2020, from https://teachmeanatomy.info/head/organs/the-nose/nasal-cavity/

39. Tsoulfanidis, N. (2011). Measurement and Detection of Radiation. Boca Raton: CRC Press, https://doi.org/10.1201/9781439894651

40. Wang, Z., Xiong, G., Tsang, W. C., Schätzlein, A. G., & Uchegbu, I. F. (2019, September 1). Nose-to-Brain Delivery. Retrieved from http://jpet.aspetjournals.org/content/370/3/593

Appendix A: MCNP Code

```
Nasal Model
c CELL CARD zz, yy, xx
c DOSE PLATES
c dose cells right
134 2 -1.000  1 -4 13 -18 221 -222 IMP:E 1 IMP:P 1  $ dose cell to right of inferior passage
135 2 -1.000  1 -4 11 -12 203 -222 IMP:E 1 IMP:P 1  $ .001 dose plate -Y
27 2 -1.000 1 -4 18 -19 219 -222 IMP:E 1 IMP:P 1  $ .001 plate top vert inferior
28 2 -1.000 1 -4 16 -19 217 -218 IMP:E 1 IMP:P 1  $ .001 plate hori vert inferior
23 2 -1.000 1 -4 15 -16 206 -219 IMP:E 1 IMP:P 1  $ .001 plate top inferior passage
34 2 -1.000 1 -4 16 -21 206 -207 IMP:E 1 IMP:P 1  $ .001 plate septum hori b inferior and middle
37 2 -1.000 1 -4 20 -21 207 -215 IMP:E 1 IMP:P 1  $ .001 plate bottom middle hori
43 2 -1.000 1 -4 20 -28 215 -216 IMP:E 1 IMP:P 1  $ .001 plate middle vert far
52 2 -1.000 1 -4 27 -28 212 -215 IMP:E 1 IMP:P 1  $ .001 plate middle vert top
49 2 -1.000 1 -4 24 -28 211 -212 IMP:E 1 IMP:P 1  $ .001 plate middle vert close
40 2 -1.000 1 -4 24 -25 207 -211 IMP:E 1 IMP:P 1  $ .001 plate top middle hori
61 2 -1.000 1 -4 29 -30 206 -209 IMP:E 1 IMP:P 1  $ .001 plate superior passage below
68 2 -1.000 1 -4 29 -34 209 -210 IMP:E 1 IMP:P 1  $ .001 plate superior far
64 2 -1.000 1 -4 33 -34 207 -209 IMP:E 1 IMP:P 1  $ .001 plate superior passage top
57 2 -1.000 1 -4 24 -29 206 -207 IMP:E 1 IMP:P 1  $ .001 plate septum hori b middle and superior
66 2 -1.000 1 -4 33 -38 206 -207 IMP:E 1 IMP:P 1  $ .001 plate septum hori above superior
163 2 -1.000 1 -4 38 -37 206 -207 IMP:E 1 IMP:P 1 $ .001 plate for deterministic effect
18 2 -1.000 1 -4 11 -38 202 -203 IMP:E 1 IMP:P 1  $ .001 plate right cartilage
164 2 -1.000 1 -4 38 -36 202 -203 IMP:E 1 IMP:P 1 $ .001 plate deterministic
9 2 -1.000 1 -4 36 -37 202 -206  IMP:E 1 IMP:P 1  $ .001 dose plate +Y >-<
c dose cells left
7 2 -1.000 1 -4 11 -12 122 -103 IMP:E 1 IMP:P 1  $ .001 plate -Y
11 2 -1.000 1 -4 12 -19 -121 122 IMP:E 1 IMP:P 1 $ .001 plate -X
79 2 -1.000 1 -4 18 -19 -118 121 IMP:E 1 IMP:P 1 $ .001 plate top vert inferior
80 2 -1.000 1 -4 15 -19 -117 118 IMP:E 1 IMP:P 1 $ .001 plate hori vert inferior
76 2 -1.000 1 -4 15 -16 -106 117 IMP:E 1 IMP:P 1 $ .001 plate top inferior passage
94 2 -1.000 1 -4 20 -21 -107 115 IMP:E 1 IMP:P 1 $ .001 plate bottom middle hori
101 2 -1.000 1 -4 20 -28 -115 116 IMP:E 1 IMP:P 1 $ .001 plate middle vert far
105 2 -1.000 1 -4 27 -28 -112 115 IMP:E 1 IMP:P 1 $ .001 plate middle vert top
104 2 -1.000 1 -4 24 -28 -111 112 IMP:E 1 IMP:P 1 $ .001 plate middle vert close
98 2 -1.000 1 -4 24 -25 -107 111 IMP:E 1 IMP:P 1 $ .001 plate top middle hori
121 2 -1.000 1 -4 29 -30 -106 109 IMP:E 1 IMP:P 1 $ .001 plate superior passage below
```

```
126 2 -1.000 1 -4 29 -34 -109 110 IMP:E 1 IMP:P 1 $ .001 plate superior far
124 2 -1.000 1 -4 33 -34 -107 109 IMP:E 1 IMP:P 1 $ .001 plate superior passage top
87 2 -1.000 1 -4 16 -21 -106 107 IMP:E 1 IMP:P 1 $ .001 plate septum hori b inferior
and middle
89 2 -1.000 1 -4 24 -29 -106 107 IMP:E 1 IMP:P 1 $ .001 plate septum hori b middle
and superior
92 2 -1.000 1 -4 33 -38 -106 107 IMP:E 1 IMP:P 1 $ .001 plate septum hori above
superior
166 2 -1.000 1 -4 38 -37 -106 107 IMP:E 1 IMP:P 1 $ .001 plate deterministic
83 2 -1.000 1 -4 11 -38 -102 103 IMP:E 1 IMP:P 1 $ .001 plate left cartilage
165 2 -1.000 1 -4 38 -37 -102 103 IMP:E 1 IMP:P 1 $ .001 plate deterministic
141 2 -1.000 1 -4 36 -37 106 -103 IMP:E 1 IMP:P 1 $.001 dose plate +Y >-<
c source cells
c structures aside from passages
1 0 -3:6:-11:37:-122:222 IMP:E,P 0 $ ultimate boundary
2 2 -1.000 1 -4 16 -20 117 -107 IMP:E 1 IMP:P 1 $ inner bound left lower
118 2 -1.000 1 -4 25 -29 111 -107 IMP:E 1 IMP:P 1 $ tissue between mid and
superior pass.
3 2 -1.000 4 -5 11 -37 122 -222 IMP:E 1 IMP:P 1 $ skin surface +Z
4 2 -1.000 5 -6 11 -37 122 -222 IMP:E 1 IMP:P 1 $ .001 plate +Z
5 2 -1.000 2 -1 11 -37 122 -222 IMP:E 1 IMP:P 1 $ skin surface -Z
6 2 -1.000 3 -2 11 -37 122 -222 IMP:E 1 IMP:P 1 $ .001 plate -Z
143 2 -1.000 1 -4 11 -12 102 -202 IMP:E 1 IMP:P 1 $ .001 plate -Y between vert sept
pass.
8 2 -1.000 1 -4 12 -13 121 -103 IMP:E 1 IMP:P 1 $ skin surface -Y
144 2 -1.000 1 -4 12 -13 102 -202 IMP:E 1 IMP:P 1 $ skin depth -Y between vert
sept pass.
136 2 -1.000 1 -4 12 -13 203 -222 IMP:E 1 IMP:P 1 $ skin depth -Y +X
152 2 -1.000 1 -4 36 -37 122 -107 IMP:E 1 IMP:P 1 $ .001 plate +Y <-
149 2 -1.000 1 -4 36 -37 102 -202 IMP:E 1 IMP:P 1 $ .001 plate between vert sept
pass.
139 2 -1.000 1 -4 36 -37 207 -222 IMP:E 1 IMP:P 1 $ .001 plate +Y ->
10 2 -1.000 1 -4 35 -36 203 -206 IMP:E 1 IMP:P 1 $ skin surface +Y >-<
142 2 -1.000 1 -4 35 -36 106 -103 IMP:E 1 IMP:P 1 $ skin depth - sept vert pass.
151 2 -1.000 1 -4 35 -36 122 -107 IMP:E 1 IMP:P 1 $ skin depth +Y -X
150 2 -1.000 1 -4 35 -36 102 -202 IMP:E 1 IMP:P 1 $ skin depth between vert sept
pass.
140 2 -1.000 1 -4 35 -36 207 -222 IMP:E 1 IMP:P 1 $ skin surface + Y ->
145 2 -1.000 1 -4 19 -35 122 -121 IMP:E 1 IMP:P 1 $ .001 plate -X above inferior
vert
12 2 -1.000 1 -4 13 -18 -120 121 IMP:E 1 IMP:P 1 $ skin surface -X
146 2 -1.000 1 -4 19 -35 121 -120 IMP:E 1 IMP:P 1 $ skin depth -X above inferior
vert
13 2 -1.000 1 -4 19 -35 221 -222 IMP:E 1 IMP:P 1 $ .001 plate +X
14 2 -1.000 1 -4 19 -35 220 -221 IMP:E 1 IMP:P 1 $ skin surface +X
```

```
133 2 -1.000 1 -4 13 -18 220 -221 IMP:E 1 IMP:P 1 $ depth inferior passage right
15 1 -1.85 1 -4 13 -35 101 -201 IMP:E 1 IMP:P 1 $ bone plate
c end of outer boundaries
c right septum passage
17 2 -1.000 1 -4 34 -35 207 -211 IMP:E 1 IMP:P 1 $ inner boundary right top
36 2 -1.000 1 -4 16 -20 207 -217 IMP:E 1 IMP:P 1 $ inner boundary right lower
16 3 -1.100 1 -4 13 -35 201 -202 IMP:E 1 IMP:P 1 $ cartilage plate right
19 2 -1.000 1 -4 13 -35 203 -204 IMP:E 1 IMP:P 1 $ skin depth right cartilage
20 0 1 -4 13 -35 204 -205 IMP:E 1 IMP:P 1 $ cavity passage hori right
33 2 -1.000 1 -4 14 -22 205 -206 IMP:E 1 IMP:P 1 $ skin depth septum hori b inferior
and middle
56 2 -1.000 1 -4 23 -30 205 -206 IMP:E 1 IMP:P 1 $ skin depth septum hori b middle
and superior
65 2 -1.000 1 -4 32 -35 205 -206 IMP:E 1 IMP:P 1 $ skin depth septum hori above
superior
c inferior passage
21 0 1 -4 13 -14 205 -220 IMP:E 1 IMP:P 1 $ inferior passage horizontal
22 2 -1.000 1 -4 14 -15 206 -219 IMP:E 1 IMP:P 1 $ skin depth top inferior passage
24 0 1 -4 14 -17 219 -220 IMP:E 1 IMP:P 1 $ inferior passage vertical
26 2 -1.000 1 -4 17 -18 219 -220 IMP:E 1 IMP:P 1 $ skin depth top vert inferior
29 2 -1.000 1 -4 16 -18 218 -219 IMP:E 1 IMP:P 1 $ skin depth hori vert inferior
31 2 -1.000 1 -4 18 -19 218 -219 IMP:E 1 IMP:P 1 $ .001 plate hori vert inferior
c doesnt matter right inferior
25 2 -1.000 1 -4 19 -35 219 -220 IMP:E 1 IMP:P 1 $ tissue above right vert path
30 2 -1.000 1 -4 19 -35 217 -218 IMP:E 1 IMP:P 1 $ tissue above dose cell hori vert
right
32 2 -1.000 1 -4 19 -35 218 -219 IMP:E 1 IMP:P 1 $ tissue above skin depth hori vert
right
c end of inferior passage
c middle passage
35 2 -1.000 1 -4 21 -22 206 -215 IMP:E 1 IMP:P 1 $ skin depth bottom middle hori
38 0 1 -4 22 -23 205 -214 IMP:E 1 IMP:P 1 $ middle passage horizontal
39 2 -1.000 1 -4 23 -24 206 -212 IMP:E 1 IMP:P 1 $ skin depth top middle hori
42 2 -1.000 1 -4 22 -27 214 -215 IMP:E 1 IMP:P 1 $ skin depth middle vert far
46 0 1 -4 23 -26 213 -214 IMP:E 1 IMP:P 1 $ middle passage vert
48 2 -1.000 1 -4 23 -27 212 -213 IMP:E 1 IMP:P 1 $ skin depth middle vert close
53 2 -1.000 1 -4 26 -27 213 -214 IMP:E 1 IMP:P 1 $ skin depth middle vert top
c doesnt matter right side middle
137 2 -1.000 1 -4 20 -21 216 -217 IMP:E 1 IMP:P 1 $ .001 plate bottom mid ->
138 2 -1.000 1 -4 21 -22 216 -217 IMP:E 1 IMP:P 1 $ skin depth bottom mid ->
41 2 -1.000 1 -4 22 -23 216 -217 IMP:E 1 IMP:P 1 $ tissue cell to right of middle
passage
44 2 -1.000 1 -4 23 -25 216 -217 IMP:E 1 IMP:P 1 $ tissue to right of depth/dose
plates
```

```
45 2 -1.000 1 -4 25 -35 216 -217 IMP:E 1 IMP:P 1 $ tissue to right of vert middle
path
47 2 -1.000 1 -4 28 -35 213 -214 IMP:E 1 IMP:P 1 $ tissue above middle vert path
50 2 -1.000 1 -4 28 -35 211 -212 IMP:E 1 IMP:P 1 $ tissue above .001 plate mid vert
close
51 2 -1.000 1 -4 28 -35 212 -213 IMP:E 1 IMP:P 1 $ tissue above skin depth mid vert
close
54 2 -1.000 1 -4 28 -35 214 -215 IMP:E 1 IMP:P 1 $ tissue above skin depth mid vert
far
55 2 -1.000 1 -4 28 -35 215 -216 IMP:E 1 IMP:P 1 $ tissue above .001 plate mid vert
far
c superior passage
58 2 -1.000 1 -4 25 -29 207 -211 IMP:E 1 IMP:P 1 $ tissue below passage
59 0 1 -4 31 -32 205 -208 IMP:E 1 IMP:P 1 $ superior passage
62 2 -1.000 1 -4 30 -31 205 -209 IMP:E 1 IMP:P 1 $ skin depth superior passage
below
63 2 -1.000 1 -4 32 -33 206 -209 IMP:E 1 IMP:P 1 $ skin depth superior passage top
67 2 -1.000 1 -4 31 -32 208 -209 IMP:E 1 IMP:P 1 $ skin depth superior far
c doesn't matter superior passage
60 2 -1.000 1 -4 31 -32 210 -211 IMP:E 1 IMP:P 1 $ superior passage right side
70 2 -1.000 1 -4 32 -33 210 -211 IMP:E 1 IMP:P 1 $ .001 plate right superior top
71 2 -1.000 1 -4 33 -34 210 -211 IMP:E 1 IMP:P 1 $ skin depth right superior top
72 2 -1.000 1 -4 30 -31 210 -211 IMP:E 1 IMP:P 1 $ skin depth right superior bottom
73 2 -1.000 1 -4 29 -30 210 -211 IMP:E 1 IMP:P 1 $ .001 plate right superior bottom
c END OF RIGHT
C --------------
C -------------
C -------------
C BEGIN LEFT
c septum left
90 3 -1.1 1 -4 13 -35 -101 102 IMP:E 1 IMP:P 1 $ cartilage plate left
84 2 -1.000 1 -4 13 -35 -103 104 IMP:E 1 IMP:P 1 $ skin depth left cartilage
85 0 1 -4 13 -35 -104 105 IMP:E 1 IMP:P 1 $ cavity passage hori left
86 2 -1.000 1 -4 14 -22 -105 106 IMP:E 1 IMP:P 1 $ skin depth septum hori b inferior
and middle
88 2 -1.000 1 -4 23 -30 -105 106 IMP:E 1 IMP:P 1 $ skin depth septum hori b middle
and superior
91 2 -1.000 1 -4 32 -35 -105 106 IMP:E 1 IMP:P 1 $ skin depth septum hori above
superior
c inferior passage left
74 0 1 -4 13 -14 -105 120 IMP:E 1 IMP:P 1 $ inferior passage horizontal
75 2 -1.000 1 -4 14 -15 -106 119 IMP:E 1 IMP:P 1 $ skin depth top inferior passage
77 0 1 -4 14 -17 -119 120 IMP:E 1 IMP:P 1 $ inferior passage vertical
78 2 -1.000 1 -4 17 -18 -119 120 IMP:E 1 IMP:P 1 $ skin depth top vert inferior
81 2 -1.000 1 -4 15 -18 -118 119 IMP:E 1 IMP:P 1 $ skin depth hori vert inferior
```

```
c doesnt matter left inferior
115 2 -1.000 1 -4 19 -35 -119 120 IMP:E 1 IMP:P 1 $ tissue above right vert path
116 2 -1.000 1 -4 19 -35 -117 118 IMP:E 1 IMP:P 1 $ tissue above dose cell hori vert
left
117 2 -1.000 1 -4 19 -35 -118 119 IMP:E 1 IMP:P 1 $ tissue above skin depth hori
vert left
c middle passage left
95 2 -1.000 1 -4 21 -22 -106 115 IMP:E 1 IMP:P 1 $ skin depth bottom middle hori
96 0 1 -4 22 -23 -105 114 IMP:E 1 IMP:P 1 $ middle passage horizontal
97 2 -1.000 1 -4 23 -24 -106 112 IMP:E 1 IMP:P 1 $ skin depth top middle hori
99 2 -1.000 1 -4 22 -27 -114 115 IMP:E 1 IMP:P 1 $ skin depth middle vert far
102 0 1 -4 23 -26 -113 114 IMP:E 1 IMP:P 1 $ middle passage vert
103 2 -1.000 1 -4 23 -27 -112 113 IMP:E 1 IMP:P 1 $ skin depth middle vert close
106 2 -1.000 1 -4 26 -27 -113 114 IMP:E 1 IMP:P 1 $ skin depth middle vert top
c doesnt matter left side middle
147 2 -1.000 1 -4 21 -22 -116 117 IMP:E 1 IMP:P 1 $ skin depth left mid pass.
148 2 -1.000 1 -4 20 -21 117 -116 IMP:E 1 IMP:P 1 $ .001 plate left mid pass
107 2 -1.000 1 -4 22 -23 -116 117 IMP:E 1 IMP:P 1 $ tissue cell to right of middle
passage
108 2 -1.000 1 -4 23 -25 -116 117 IMP:E 1 IMP:P 1 $ tissue to right of depth/dose
plates
109 2 -1.000 1 -4 25 -35 -116 117 IMP:E 1 IMP:P 1 $ tissue to right of vert middle
path
110 2 -1.000 1 -4 28 -35 -113 114 IMP:E 1 IMP:P 1 $ tissue above middle vert path
111 2 -1.000 1 -4 28 -35 -111 112 IMP:E 1 IMP:P 1 $ tissue above .001 plate mid
vert close
112 2 -1.000 1 -4 28 -35 -112 113 IMP:E 1 IMP:P 1 $ tissue above skin depth mid
vert close
113 2 -1.000 1 -4 28 -35 -114 115 IMP:E 1 IMP:P 1 $ tissue above skin depth mid
vert far
114 2 -1.000 1 -4 28 -35 -115 116 IMP:E 1 IMP:P 1 $ tissue above .001 plate mid
vert far
c superior left
120 0 1 -4 31 -32 -105 108 IMP:E 1 IMP:P 1 $ superior passage
122 2 -1.000 1 -4 30 -31 -105 109 IMP:E 1 IMP:P 1 $ skin depth superior passage
below
123 2 -1.000 1 -4 32 -33 -106 109 IMP:E 1 IMP:P 1 $ skin depth superior passage top
125 2 -1.000 1 -4 31 -32 -108 109 IMP:E 1 IMP:P 1 $ skin depth superior far
c dont matta
132 2 -1.000 1 -4 34 -35 111 -107 IMP:E 1 IMP:P 1 $ tissue above superior passage
127 2 -1.000 1 -4 31 -32 -110 111 IMP:E 1 IMP:P 1 $ superior passage left side
128 2 -1.000 1 -4 32 -33 -110 111 IMP:E 1 IMP:P 1 $ .001 plate left superior top cont
129 2 -1.000 1 -4 33 -34 -110 111 IMP:E 1 IMP:P 1 $ skin depth left superior top
cont
```

130 2 -1.000 1 -4 30 -31 -110 111 IMP:E 1 IMP:P 1 $ skin depth cont left superior below
131 2 -1.000 1 -4 29 -30 -110 111 IMP:E 1 IMP:P 1 $ .001 plate left superior cont below

c SURFACE CARD
c START Z SURFACES
1 pz -2.5
2 pz -2.502
3 pz -2.503
4 pz 2.5
5 pz 2.502
6 pz 2.503
c END OF Z SURFACES
11 py -2.003 $ base of model 10 micron
12 py -2.002 $ base of model 10 micron
13 py -2 $ BASE OF MODEL------
14 py -1.7 $ TOP INFERIOR PATH------
15 py -1.698 $ top inferior path 10 micron
16 py -1.697 $ top inferior path 10 micron
17 py -1.5 $ TOP INFERIOR VERTICAL------
18 py -1.498 $ top inferior vertical 10 micron
19 py -1.497 $ top inferior vertical 10 micron
20 py 0.497 $ bottom middle path 10 micron
21 py 0.498 $ bottom middle path 10 micron
22 py 0.5 $ BOTTOM MIDDLE PATH-------
23 py 0.7 $ TOP MIDDLE PATH---------
24 py 0.702 $ top middle path 10 micron
25 py 0.703 $ top middle path 10 micron
26 py 0.9 $ TOP MIDDLE VERTICAL-----------
27 py 0.902 $ top middle vertical 10 micron
28 py 0.903 $ top middle vertical 10 micron
29 py 1.697 $ bottom superior path 10 micron
30 py 1.698 $ bottom superior path 10 micron
31 py 1.7 $ BOTTOM SUPERIOR PATH--------
32 py 1.8034 $ TOP SUPERIOR PATH------
33 py 1.8054 $ top superior path 10 micron
34 py 1.8064 $ top superior path 10 micron
35 py 3 $ TOP OF MODEL-------
36 py 3.002 $ top of model 10 micron
37 py 3.003 $ top of model 10 micron
38 py 2.5 $ dose cell
c END OF Y SURFACES
c START NEGATIVE X SURFACES
101 px -0.05 $ BONE-------

```
102 px -0.15 $ CARTILAGE------
103 px -0.151 $ 10 micron
104 px -0.153 $ HORI WALL NEAR------
105 px -0.453 $ HORI WALL FAR------
106 px -0.455 $ 10 micron
107 px -0.456 $ 10 micron
108 px -0.743 $ SUPERIOR WALL------
109 px -0.745 $ 10 micron
110 px -0.746 $ 10 micron
111 px -0.85 $ 10 micron
112 px -0.851 $ 10 micron
113 px -0.853 $ MIDDLE WALL CLOSE------
114 px -1.053 $ MIDDLE WALL FAR------
115 px -1.055 $ 10 micron
116 px -1.056 $ 10 micron
117 px -1.15 $ 10 micron
118 px -1.151 $ 10 micron
119 px -1.153 $ INFERIOR WALL CLOSE------
120 px -1.453 $ INFERIOR WALL FAR-------
121 px -1.455 $ 10 micron
122 px -1.456 $ 10 micron
c END NEGATIVE SURFACES
c BEGIN POSITIVE SURFACES
201 px 0.05 $ BONE
202 px 0.15 $ CARTILAGE
203 px 0.151 $ 10 micron
204 px 0.153 $ HORI WALL NEAR
205 px 0.453 $ HORI WALL FAR
206 px 0.455 $ 10 micron
207 px 0.456 $ 10 micron
208 px 0.743 $ SUPERIOR WALL
209 px 0.745 $ 10 micron
210 px 0.746 $ 10 micron
211 px 0.85 $ 10 micron
212 px 0.851 $ 10 micron
213 px 0.853 $ MIDDLE WALL CLOSE
214 px 1.053 $ MIDDLE WALL FAR
215 px 1.055 $ 10 micron
216 px 1.056 $ 10 micron
217 px 1.150 $ 10 micron
218 px 1.151 $ 10 micron
219 px 1.153 $ INFERIOR WALL CLOSE
220 px 1.453 $ INFERIOR WALL FAR
221 px 1.455 $ 10 micron
222 px 1.456 $ 10 micron
```

```
C END OF X SURFACES

c DATA CARD
MODE E P
PHYS:P
PHYS:E 0.7
SDEF PAR=f erg=d5 x=d1 y=d2 z=d3 cel=d4
SI1 -1.5 1.5
SP1 0 1
SI2 -2.2 3.1
SP2 0 1
SI3 -2.6 2.6
SP3 0 1
SI4 L 85 20
SP4 0.5 0.5
SI5 L 0.0159 0.0475 0.0792 0.1109 0.1426 0.1742 0.2059 0.2376 0.2693 0.3009
     0.3643 0.3960 0.4276 0.4593 0.4910 0.5227 0.5543 0.5860 0.6177
SP5  1.86E-02 4.54E-02 6.21E-02 7.33E-02 8.05E-02 8.44E-02 8.55E-02 8.43E-02
    8.08E-02 7.55E-02 6.87E-02 6.08E-02 5.19E-02 4.25E-02 3.31E-02 2.40E-02
    8.64E-03 3.32E-03 6.08E-04
M1   1000 -0.047234 $ bone density -1.850000
    6000 -0.144330
    7000 -0.041990
    8000 -0.446096
    12000 -0.002200
    15000 -0.104970
    16000 -0.003150
    20000 -0.209930
    30000 -0.000100
M2   1000 -0.104472 $ tissue density -1.0000
    6000 -0.232190
    7000 -0.024880
    8000 -0.630238
    11000 -0.001130
    12000 -0.000130
    15000 -0.001330
    16000 -0.001990
    17000 -0.001340
    19000 -0.001990
    20000 -0.000230
    26000 -0.000050
    30000 -0.000030
M3   1001 -.096  $ cartilage density -1.1
    6000 -.099
    7014 -.022
```

```
    8016 -.744s
    11023 -.005
    15031 -.022
    16000 -.009
    17000 -.003
*F8:E (134 135 27 28 23 34 37 43 52 49 40 61 68 64 57 66 18 9 163 164 7 11 79 80
     76 94 101 105 104 98 121 126 124 87 89 92 83 141 166 165)
*F18:E (134 135 27 28 23 34 37 43 52 49 40 61 68 64 57 66 18 9 163 164)
*F28:E (7 11 79 80 76 94 101 105 104 98 121 126 124 87 89 92 83 141 166 165)
NPS 1000000
```